

AstroGK: Astrophysical Gyrokinetics Code

Ryusuke Numata^{a,b,*}, Gregory G. Howes^c, Tomoya Tatsuno^a, Michael Barnes^{d,e}, William Dorland^a

^a*CSCAMM & IREAP, University of Maryland, College Park, MD 20742, USA.*

^b*Wolfgang Pauli Institute, University of Vienna, A-1090 Vienna, Austria*

^c*Department of Physics and Astronomy, University of Iowa, Iowa City, IA 52242, USA.*

^d*Rudolf Peierls Centre for Theoretical Physics, University of Oxford, Oxford OX1 3NP, UK.*

^e*Euratom/CCFE Fusion Association, Culham Science Centre, Abingdon OX14 3DB, UK.*

Abstract

The gyrokinetic simulation code **AstroGK** is developed to study fundamental aspects of kinetic plasmas and for applications mainly to astrophysical problems. **AstroGK** is an Eulerian slab code that solves the electromagnetic gyrokinetic-Maxwell equations in five-dimensional phase space, and is derived from the existing gyrokinetics code **GS2** by removing magnetic geometry effects. Algorithms used in the code are described. The code is benchmarked using linear and nonlinear problems. Serial and parallel performance scalings are also presented.

Keywords: Gyrokinetic simulation, Eulerian, Numerical Methods

PACS: 52.30.Gz, 52.65.Tt, 94.05.-a, 95.30.Qd

*Corresponding author at: CSCAMM & IREAP, University of Maryland, College Park, MD 20742, USA. Tel.: +1 301 405 1608; fax: +1 301 405 1678.

Email address: rnumata@umd.edu (Ryusuke Numata)

1. Introduction

Gyrokinetics is a limit of kinetic theory that describes the low-frequency dynamics of weakly collisional plasmas in a mean magnetic field. Developed for the study of magnetically confined fusion plasmas, it has proven to be a valuable tool in understanding the dynamics of drift-wave turbulence, a key cause of the enhanced transport measured in modern fusion experiments that leads to poor device performance. Tremendous theoretical, computational, and experimental efforts have been devoted to this problem, with steady progress over three decades.

It has been recently recognized that the gyrokinetic approach is also well-suited to the study of astrophysical plasmas, including galaxy clusters, accretion disks around compact objects, the interstellar medium, and the solar corona and solar wind [1–3]. Taking advantage of the knowledge and computational techniques developed in the simulation of turbulence in fusion plasmas, **AstroGK** [4], a gyrokinetic simulation code, is developed specifically for the study of astrophysical problems. In this paper, we describe the algorithms employed in **AstroGK** and present verification tests and performance results.

Gyrokinetics describes the low-frequency fluctuations of magnetized plasmas by exploiting the timescale separation between the low-frequency dynamics of interest and the fast cyclotron motion of particles, $\omega \ll \Omega$, where ω is the typical frequency of fluctuations and Ω is the cyclotron frequency. By averaging the kinetic Vlasov–Landau (or Boltzmann) equation and Maxwell’s equations over the fast cyclotron motion, a self-consistent gyrokinetic-Maxwell (GK-M) system is defined in five-dimensional phase space. This system orders out the fast MHD waves and the cyclotron resonance, but retains finite Larmor radius (FLR) effects and collisionless wave-particle interactions via the Landau resonance [5, 6].

The theoretical foundation of gyrokinetics has been developed extensively over the past four decades [1, 7–17], and gyrokinetics is now broadly employed for numerical studies of turbulence driven by microinstabilities in laboratory plasmas. The reduction of the phase-space dimensionality and the relaxed timestep constraints under the gyrokinetic approximation have made possible gyrokinetic simulations of fusion devices, yet it is still computationally demanding. The simulation of the kinetic dynamics of magnetized plasmas in both laboratory and astrophysical settings presents a challenge to the scientific community requiring the most advanced computing technology available.

A number of computational codes for gyrokinetics have been developed and are actively refined worldwide by the fusion community [18–26]. These codes are typically classified by the following characteristics: Eulerian continuum vs. Lagrangian particle (PIC), local flux tube vs. global toroidal, δf vs. full- f , and electromagnetic vs. electrostatic. **AstroGK** has been derived from the Eulerian continuum, local flux tube, δf , electromagnetic code **GS2** [18, 20]. **GS2** was designed to simulate plasma dynamics in fusion devices where the magnetic geometry plays a central role. The handling in the code of the toroidal magnetic geometry and of particle trapping requires a rather complicated numerical implementation. In contrast, the study of the fundamental properties of kinetic plasmas for application to astrophysical situations demands the simulation of the dynamics at scales of order the particle Larmor radii on which the magnetic field is well approximated as straight or gently curved, so the coding to handle complicated magnetic geometries is unnecessary. Therefore **AstroGK** was created by stripping **GS2** of the cumbersome coding necessary to describe the magnetic geometry effects, leading to a simplified, faster code ideally suited to study weakly collisional astrophysical plasmas. In addition to this, we believe the code is also an ideal testbed for new ideas of additional physics, diagnostics, numerical algorithms, and optimizations which may be exported back to **GS2**.

AstroGK has already proven its usefulness in a number of studies. For example, it has produced the first kinetic simulations of turbulence describing the transition from Alfvén to kinetic Alfvén wave turbulence at the scale of the ion Larmor radius in an attempt to understand solar wind turbulence [27], revealed nonlinear phase-mixing properties of turbulence [28], enabled the study of the statistical properties of phase-space structures of plasma turbulence [29], explored the transition from collisional to collisionless tearing instabilities [30], and described the Alfvén wave dynamics in the LAPD experiment [31].

This paper is organized as follows: In Section 2, the set of GK-M equations solved in the code is given. Section 3 describes algorithms employed in the code, including the velocity-space discretization and integration, the finite-difference formalism of the GK-M system along the mean field direction and its

solution by the special technique developed by Kotschenreuther et al. [18], the parallelization scheme, and some additional features of the code. Section 4 presents tests of **AstroGK**, ranging from linear electrostatic problems to nonlinear fully electromagnetic problems. Comparisons to analytic solutions of the linear problems enable the verification of the code and nonlinear examples show potential ability to apply the code to complicated problems. Serial and parallel performance measurements of the code on cutting edge supercomputers are given in Section 5. In Section 6, we present a summary of the paper.

2. Gyrokinetic-Maxwell equations

In this section, we present the gyrokinetic-Maxwell (GK-M) system of equations solved in **AstroGK**. For notational simplicity, we summarize all the symbols and their definitions in Appendix A.

We first assume that scale separations in space and time are well satisfied such that small fluctuations are locally embedded in a background plasma which is slowly varying spatially and temporally. We consider a temporally constant mean magnetic field $\mathbf{B}_0 = B_0 \hat{\mathbf{b}}_0$. The mean field is pointing almost parallel to $\hat{\mathbf{z}}$, but is allowed to have curvature $\kappa = |(\hat{\mathbf{b}}_0 \cdot \nabla) \hat{\mathbf{b}}_0|$. We also assume the amplitude of the mean field is constant along its direction, $\hat{\mathbf{b}}_0 \cdot \nabla B_0 = 0$, but has finite gradient perpendicular to its direction, $\hat{\mathbf{b}}_0 \times \nabla B_0 \neq 0$. Under this assumption, particle trapping do not take place. In the presence of a mean magnetic field, we can adopt the gyrokinetic ordering and average over the fast cyclotron motion to reduce the Vlasov–Maxwell equations to the GK-M equations; see Howes et al. [1] and Schekochihin et al. [3] for derivations of these equations expressly intended for the study of astrophysical plasmas.

Under the gyrokinetic ordering, the distribution function of particles up to the first order is given by

$$f_s = \left(1 - \frac{q_s \phi}{T_{0s}} + \frac{\mathbf{v} \times \hat{\mathbf{z}}}{\Omega_s} \cdot \nabla_{\perp} \right) f_{0s} + h_s, \quad (1)$$

where $f_{0s} = n_{0s}/(\sqrt{\pi}v_{\text{th},s})^3 \exp(-v^2/v_{\text{th},s}^2)$ is the zeroth-order, equilibrium Maxwellian distribution function. The first-order part of the distribution function is composed of the Boltzmann response term, a term due to gradients of the equilibrium, and the gyro-center distribution function h_s defined in the gyro-center coordinate $(\mathbf{R}_s, \mathbf{V}_s)$.¹ Upon averaging over the gyro-phase, the gyrokinetic equation evolves $h_s = h_s(X_s, Y_s, Z_s, V_{\parallel,s}, V_{\perp,s}, t)$:

$$\frac{\partial h_s}{\partial t} + V_{\parallel,s} \frac{\partial h_s}{\partial Z_s} + \mathbf{v}_{\text{D},s} \cdot \left(\frac{\partial h_s}{\partial \mathbf{R}_s} + \hat{\mathbf{X}}_s \frac{\partial f_{0s}}{\partial X_s} \right) = \frac{q_s f_{0s}}{T_{0s}} \frac{\partial \langle \chi \rangle_{\mathbf{R}_s}}{\partial t} + C(h_s), \quad (2)$$

where parallel and perpendicular subscripts refer to directions with respect to the mean magnetic field. The perpendicular drift velocity is given by

$$\mathbf{v}_{\text{D},s} = -\hat{\mathbf{Y}}_s \frac{V_{\perp,s}^2}{2\Omega_s} L_{B_0}^{-1} - \hat{\mathbf{Y}}_s \frac{V_{\parallel,s}^2}{\Omega_s} \kappa - \frac{\partial \langle \chi \rangle_{\mathbf{R}_s}}{\partial \mathbf{R}_s} \times \frac{\hat{\mathbf{Z}}_s}{B_0}, \quad (3)$$

where the terms correspond, from left to right, to the gradient- B drift ($L_{B_0}^{-1} \equiv -\partial \ln B_0 / \partial X_s$), the curvature drift, and a *nonlinear* drift.² We have taken the direction of the gradients of B_0 and f_{0s} and the curvature in the $-\hat{\mathbf{X}}_s$ direction. The gyrokinetic potential is given by $\chi = \phi - \mathbf{v} \cdot \mathbf{A}$, and the linear collision term is represented by $C(h_s)$. The angle bracket $\langle \cdot \rangle_{\mathbf{R}_s}$ denotes the gyro-average at fixed gyro-center coordinate \mathbf{R}_s :

$$\langle F(\mathbf{r}) \rangle_{\mathbf{R}_s} = \frac{1}{2\pi} \oint F \left(\mathbf{R}_s + \frac{\mathbf{V}_s \times \hat{\mathbf{Z}}_s}{\Omega_s} \right) d\Theta_s, \quad (4)$$

where $\mathbf{V}_s = (V_{\perp,s}, V_{\parallel,s}, \Theta_s)$. (The gyro-average at fixed particle coordinate $\langle \cdot \rangle_{\mathbf{r}}$ can also be defined by switching roles of \mathbf{r} and \mathbf{R}_s .)

In the GK-M system, the electromagnetic fields are specified by the three scalar functions $\phi(\mathbf{r}, t)$, $A_{\parallel}(\mathbf{r}, t)$, and $\delta B_{\parallel}(\mathbf{r}, t)$ ³ according to:

$$\mathbf{B} = \nabla_{\perp} A_{\parallel} \times \hat{\mathbf{z}} + \delta B_{\parallel} \hat{\mathbf{z}}, \quad \mathbf{E} = -\nabla \phi - \frac{\partial \mathbf{A}}{\partial t}. \quad (5)$$

¹ $\mathbf{V}_s = \mathbf{v}$, and, normally, is not distinguished from \mathbf{v} . See Appendix A.1.

² ϕ , $V_{\parallel} A_{\parallel}$, and $\mathbf{V}_{\perp} \cdot \mathbf{A}_{\perp}$ terms in χ yield the $\mathbf{E} \times \mathbf{B}$ drift, a parallel streaming along the perturbed magnetic field, and the ∇B drift due to δB_{\parallel} , respectively.

³ $\delta B_{\parallel} = (\nabla_{\perp} \times \mathbf{A}_{\perp})_z$. We use the Coulomb gauge, which leads to $\nabla_{\perp} \cdot \mathbf{A}_{\perp} = 0$ with the ordering. Then, we can write $\mathbf{A}_{\perp} = \nabla_{\perp} \zeta \times \hat{\mathbf{z}}$, and $\delta B_{\parallel} = -\nabla_{\perp}^2 \zeta$ in terms of a single scalar function ζ .

Maxwell's equations in the gyrokinetic limit reduce to the quasi-neutrality condition, and the parallel and perpendicular components of Ampère's law:

$$\sum_s \left[-\frac{q_s^2 n_{0s}}{T_{0s}} \phi + q_s \int \langle h_s \rangle_{\mathbf{r}} d\mathbf{v} \right] = 0, \quad (6)$$

$$-\nabla_{\perp}^2 A_{\parallel} = \mu_0 \sum_s q_s \int \langle V_{\parallel,s} h_s \rangle_{\mathbf{r}} d\mathbf{v}, \quad (7)$$

$$B_0 \nabla_{\perp} \delta B_{\parallel} = -\mu_0 \nabla_{\perp} \cdot \sum_s q_s \int \langle m \mathbf{V}_{\perp,s} \mathbf{V}_{\perp,s} h_s \rangle_{\mathbf{r}} d\mathbf{v}. \quad (8)$$

To lowest order, the quasi-neutrality condition and the perpendicular Ampère's law imply the constraints on the background plasma of quasi-neutrality and total pressure balance:

$$\sum_s n_{0s} q_s = 0, \quad \frac{\partial}{\partial X_s} \left(\frac{B_0^2}{2\mu_0} + \sum_s n_{0s} T_{0s} \right) = 0. \quad (9)$$

It is advantageous, both analytically and in the code, to Fourier transform the equations only in the plane perpendicular to the mean magnetic field. The distribution function and the fields are decomposed as

$$h_s(X_s, Y_s, Z_s, V_{\parallel,s}, V_{\perp,s}, t) = \sum_{\mathbf{k}_{\perp}} h_{s,\mathbf{k}_{\perp}}(Z_s, V_{\parallel,s}, V_{\perp,s}, t) e^{i\mathbf{k}_{\perp} \cdot \mathbf{R}_s}, \quad (10)$$

$$\phi(x, y, z, t) = \sum_{\mathbf{k}_{\perp}} \phi_{\mathbf{k}_{\perp}}(z, t) e^{i\mathbf{k}_{\perp} \cdot \mathbf{r}} \quad (11)$$

with $\mathbf{k}_{\perp} = (k_x, k_y, 0)$. The virtue of expressing variables in Fourier space is that the gyro-averaging operation becomes a multiplication by a Bessel function. For example, the gyro-average of the gyrokinetic potential is given by

$$\langle \chi \rangle_{\mathbf{R}_s} = \sum_{\mathbf{k}_{\perp}} \left[J_0(\alpha_s) (\phi_{\mathbf{k}_{\perp}} - V_{\parallel,s} A_{\parallel,\mathbf{k}_{\perp}}) + \frac{T_{0s}}{q_s} \frac{2V_{\perp,s}^2}{v_{\text{th},s}^2} \frac{J_1(\alpha_s)}{\alpha_s} \frac{\delta B_{\parallel,\mathbf{k}_{\perp}}}{B_0} \right] e^{i\mathbf{k}_{\perp} \cdot \mathbf{R}_s}, \quad (12)$$

where J_n is the Bessel function of the first kind with the argument $\alpha_s = k_{\perp} V_{\perp,s} / \Omega_s$, taking $k_{\perp} = |\mathbf{k}_{\perp}|$. The Fourier coefficients of the fields are now functions of Z_s and t , for example $\phi_{\mathbf{k}_{\perp}} = \phi_{\mathbf{k}_{\perp}}(Z_s, t)$.

In the large-scale limit $k_{\perp} \rho_i \ll 1$, Alfvénic perturbations have a gyro-center distribution function h_s that is largely canceled by the Boltzmann response term $(q_s \phi / T_{0s}) f_{0s}$ (see, for example, Section 5 of [3]). To avoid numerical error arising from this near cancellation, a complementary distribution function g_s is introduced, given by

$$g_s = h_s - \frac{q_s f_{0s}}{T_{0s}} \langle \phi - \mathbf{v}_{\perp} \cdot \mathbf{A}_{\perp} \rangle_{\mathbf{R}_s}. \quad (13)$$

After normalization described in Appendix A.2, we finally obtain a normalized version of the GK-M equations as follows. The normalized gyrokinetic equation is

$$\begin{aligned} \frac{\partial g_{\mathbf{k}_{\perp},s}}{\partial t} + \sqrt{\frac{T_{0s}}{m_s}} V_{\parallel,s} \frac{\partial h_{\mathbf{k}_{\perp},s}}{\partial Z_s} + \frac{1}{2} \mathcal{F}(\{\langle \chi \rangle_{\mathbf{R}_s}, h_s\}) \\ + \frac{ik_y}{2} \left[-\frac{T_{0s}}{q_s} (V_{\perp,s}^2 L_{B_0}^{-1} + 2V_{\parallel,s}^2 \kappa) h_{\mathbf{k}_{\perp},s} + \left(L_{n_{0s}}^{-1} + \left(V_s^2 - \frac{3}{2} \right) L_{T_{0s}}^{-1} \right) \langle \chi \rangle_{\mathbf{R}_s, \mathbf{k}_{\perp}} \right] \\ = -\frac{q_s}{\sqrt{m_s T_{0s}}} V_{\parallel,s} J_0(\alpha_s) \frac{\partial A_{\parallel,\mathbf{k}_{\perp}}}{\partial t} + C_{\mathbf{k}_{\perp}}(h_{\mathbf{k}_{\perp},s}), \end{aligned} \quad (14)$$

where $V_s^2 = V_{\perp,s}^2 + V_{\parallel,s}^2$ and the normalized gyrokinetic potential is

$$\langle \chi \rangle_{\mathbf{R}_s} = \sum_{\mathbf{k}_{\perp}} \left[J_0(\alpha_s) \phi_{\mathbf{k}_{\perp}} - \sqrt{\frac{T_{0s}}{m_s}} V_{\parallel,s} J_0(\alpha_s) A_{\parallel,\mathbf{k}_{\perp}} + \frac{T_{0s}}{q_s} 2V_{\perp,s}^2 \frac{J_1(\alpha_s)}{\alpha_s} \delta B_{\parallel,\mathbf{k}_{\perp}} \right] e^{i\mathbf{k}_{\perp} \cdot \mathbf{R}_s}. \quad (15)$$

The nonlinear term, given by the Poisson bracket $\{a, b\} = (\partial a / \partial X_s)(\partial b / \partial Y_s) - (\partial b / \partial X_s)(\partial a / \partial Y_s)$, is evaluated in real space and then transformed into Fourier space (denoted by \mathcal{F}). The terms in the gyrokinetic equation due to gradients of the background plasma, given in square brackets, contribute at the same order as the other terms, and are characterized by the parameters $L_{B_0}^{-1}$, $L_{n_{0s}}^{-1} \equiv -\partial \ln n_{0s} / \partial X_s$, $L_{T_{0s}}^{-1} \equiv -\partial \ln T_{0s} / \partial X_s$, and the curvature κ . The normalized Maxwell's equations are

$$\phi_{\mathbf{k}_\perp} \sum_s \frac{n_{0s} q_s^2}{T_{0s}} (1 - \Gamma_{0s}) - \delta B_{\parallel, \mathbf{k}_\perp} \sum_s q_s n_{0s} \Gamma_{1s} = \sum_s q_s \mathcal{M}^{(0)}(g_{\mathbf{k}_\perp, s}), \quad (16)$$

$$\frac{k_\perp^2}{2\beta_0} A_{\parallel, \mathbf{k}_\perp} = \sum_s q_s n_{0s} \mathcal{M}^{(1)}(g_{\mathbf{k}_\perp, s}), \quad (17)$$

$$\phi_{\mathbf{k}_\perp} \sum_s q_s n_{0s} \Gamma_{1s} + \delta B_{\parallel, \mathbf{k}_\perp} \left(\frac{2}{\beta_0} + \sum_s n_{0s} T_{0s} \Gamma_{2s} \right) = - \sum_s \mathcal{M}^{(2)}(g_{\mathbf{k}_\perp, s}). \quad (18)$$

The plasma beta of the reference species, defined by the ratio of the thermal pressure of the reference species to the magnetic pressure of the mean magnetic field, is given by β_0 . The operators $\mathcal{M}^{(n)}$ to take the n th order moment of the distribution function are:

$$\mathcal{M}^{(0)}(g_{\mathbf{k}_\perp, s}) = n_{0s} \int g_{\mathbf{k}_\perp, s} J_0(\alpha_s) \frac{e^{-v_s^2}}{\pi^{3/2}} d\mathbf{v}_s, \quad (19)$$

$$\mathcal{M}^{(1)}(g_{\mathbf{k}_\perp, s}) = \sqrt{\frac{T_{0s}}{m_s}} \int g_{\mathbf{k}_\perp, s} v_{\parallel, s} J_0(\alpha_s) \frac{e^{-v_s^2}}{\pi^{3/2}} d\mathbf{v}_s, \quad (20)$$

$$\mathcal{M}^{(2)}(g_{\mathbf{k}_\perp, s}) = n_{0s} T_{0s} \int g_{\mathbf{k}_\perp, s} v_{\perp, s}^2 \frac{2J_1(\alpha_s)}{\alpha_s} \frac{e^{-v_s^2}}{\pi^{3/2}} d\mathbf{v}_s. \quad (21)$$

The function $\Gamma_{ns} = \Gamma_n(b_s)$ arises from the integration over perpendicular velocity space of products of two Bessel functions. For $n = 0, 1, 2$, it is given by

$$\Gamma_0(b_s) = I_0(b_s) e^{-b_s}, \quad \Gamma_1(b_s) = (I_0(b_s) - I_1(b_s)) e^{-b_s}, \quad \Gamma_2(b_s) = 2\Gamma_1(b_s) \quad (22)$$

where I_n is the modified Bessel function of the first kind, and the argument is $b_s = (k_\perp \rho_s)^2 / 2$ [1].

The background plasma must also satisfy the normalized quasi-neutrality and total pressure balance constraints:

$$\sum_s n_{0s} q_s = 0, \quad L_{B_0}^{-1} + \frac{\beta_0}{2} \sum_s n_{0s} T_{0s} (L_{n_{0s}}^{-1} + L_{T_{0s}}^{-1}) = 0. \quad (23)$$

We defer description of the explicit form of the collision operator used in the code to Appendix B, as it has a rather cumbersome form and is fully documented in [32]. We mention here the basic properties of the operator. The operator is based on the linearized Landau collision operator transformed into the gyro-center coordinate. It has second-order velocity derivatives providing diffusion in velocity space and *conserving terms* which include integrations over velocity space. It is constructed to satisfy Boltzmann's H -theorem and the conservation of particles, momentum, and energy. It contains both like-species collisions and inter-species collisions, but the inter-species collisions account only for the collisions of electrons with one species of ions with large mass. Note that the linearized collision operator for a given species can be made independent of the first-order evolution of any other species. The theoretical basis of the collision operator is discussed in detail in [33].

3. Algorithm description

This section describes the numerical algorithms used in **AstroGK** to evolve the GK-M system of Eqs. (14), and (16)–(18). The gyrokinetic equation combined with the field equations together comprise a set of integro-differential equations for the evolution of the distribution function g defined in the five-dimensional phase space $(X, Y, Z, V_{\parallel}, V_{\perp})$. In this section, the species subscript s is omitted unless necessary. Periodic boundary conditions are assumed for the spatial dimensions (X, Y, Z) , and the derivatives in the plane perpendicular to the mean field, (X, Y) , are handled using a Fourier-spectral method. Except for the nonlinear term, each Fourier mode is independent of the others in the gyrokinetic equation, so we omit the \mathbf{k}_{\perp} subscript for simplicity. In the numerical implementation described here, because fields are calculated separately from the gyrokinetic equations, the gyrokinetic equation for each species is essentially independent of that for the other species. The mean field parallel direction Z and the time t are discretized by $Z_i = i\Delta Z$ ($i = 0, \dots, N_Z$) and $t_n = \sum_{j=1}^n \Delta t_j$, where ΔZ is fixed and Δt_j may vary to satisfy the Courant–Friedrichs–Lewy (CFL) condition [34] for the nonlinear term. Velocity space is discretized with grid points chosen by Gaussian quadrature rules for optimal integration, generating nonuniform meshes.

3.1. Velocity-space integration

The velocity grid in **AstroGK** is specified by (λ, E, σ) , where the pitch angle⁴ is $\lambda = v_{\perp}^2/v^2$, the energy is $E = v_{\perp}^2 + v_{\parallel}^2$, and the sign of parallel velocity is $\sigma = \text{sgn}(v_{\parallel})$. The velocity-space integral to calculate moments is represented by an integration of some function $F(\lambda, E, \sigma, \dots)$ multiplied by the Maxwellian e^{-E} :

$$\int F e^{-E} d\mathbf{v} = \pi \sum_{\sigma=\pm 1} \int_0^{\infty} e^{-E} \sqrt{E} dE \int_0^1 \frac{d\lambda}{\sqrt{1-\lambda}} F(\lambda, E, \sigma, \dots). \quad (24)$$

Gaussian quadrature evaluates an integral of a function $F(x)$ with weight $W(x)$ by

$$\int_a^b W(x) F(x) dx \approx \sum_{j=1}^N w_j F(x_j), \quad (25)$$

where x_j is the j th root of the N th order polynomial, and w_j is the corresponding discretized weight. The weights for the Gauss–Legendre and Gauss–Laguerre rules are given by

$$w_j^{\text{Leg}} = \frac{2}{\left(1 - \left(x_j^{\text{Leg}}\right)^2\right) \left(P'_N \left(x_j^{\text{Leg}}\right)\right)^2}, \quad w_j^{\text{Lag}} = \frac{x_j^{\text{Lag}}}{(N+1)^2 \left(L_{N+1} \left(x_j^{\text{Lag}}\right)\right)^2}, \quad (26)$$

where P_N and L_N are the N th order Legendre and Laguerre polynomials, respectively [35]. The superscripts ‘Leg’ and ‘Lag’ to x_j and w_j explicitly denote that they are associated with the Gauss–Legendre and Gauss–Laguerre rules. The weight function $W(x)$ and the integration range are chosen according to the polynomial.

For the pitch-angle integration, the Gauss–Legendre quadrature ($a = -1$, $b = 1$, $W(x) = 1$) is immediately applied by defining $\xi = \sqrt{1-\lambda}$:

$$\begin{aligned} \int_0^1 F(\lambda, \dots) \frac{d\lambda}{\sqrt{1-\lambda}} &= 2 \int_0^1 F(1-\xi^2, \dots) d\xi \\ &\approx \sum_{j=1}^{N_{\lambda}} w_j^{\text{Leg}} F \left(1 - \left(\frac{x_j^{\text{Leg}} + 1}{2} \right)^2, \dots \right). \end{aligned} \quad (27)$$

⁴The pitch-angle parameter λ is used for historical reasons. If the magnitude of the mean magnetic field changes along its direction, particles may be trapped in magnetic wells. Trapped and untrapped regions in velocity space are conveniently described by the λ coordinate [18]. Since **AstroGK** does not contain this physics, the use of λ is not necessary, but is inherited from **GS2**. The pitch-angle variable $\xi = v_{\parallel}/v$ could be used instead.

The integration range is changed using a linear transformation to fit the range of the Gauss–Legendre rule. N_λ is the number of grid points describing the λ grid and is specified by the user input, `ngauss`: $N_\lambda = 2 \times \text{ngauss}$.

A rather careful treatment of the energy integral is necessary because there are singularities of the integrand at $E = 0$ and $E = \infty$ which may prevent a simple approximation from achieving spectral convergence. To avoid the problem, we split the integration range at $E_{\text{cut}} = v_{\text{cut}}^2$ into a lower and an upper range and change the variable to v from E for the lower range integration: the Gauss–Legendre scheme is used for the lower range; and the Gauss–Laguerre ($a = 0$, $b = \infty$, $W(x) = e^{-x}$) is used for the upper range. Therefore, the integration is approximated by

$$\begin{aligned} \int_0^\infty F(E, \dots) e^{-E} \sqrt{E} dE &= \int_0^{v_{\text{cut}}} F(v^2, \dots) e^{-v^2} 2v^2 dv + \int_{E_{\text{cut}}}^\infty F(E, \dots) e^{-E} \sqrt{E} dE \\ &\approx \frac{v_{\text{cut}}}{2} \sum_{j=1}^{N_E^-} w_j^{\text{Leg}} G_1 \left(\frac{v_{\text{cut}}}{2} \left(x_j^{\text{Leg}} + 1 \right), \dots \right) \\ &\quad + e^{-E_{\text{cut}}} \sum_{j=1}^{N_E^+} w_j^{\text{Lag}} G_2 \left(x_j^{\text{Lag}} + E_{\text{cut}}, \dots \right), \end{aligned} \quad (28)$$

where

$$G_1(x) = F(x^2, \dots) e^{-x^2} 2x^2, \quad G_2(x) = F(x, \dots) \sqrt{x}, \quad (29)$$

and the integration ranges are shifted appropriately. We allow users to specify $v_{\text{cut}} = \text{vcut}$, $N_E^- = \text{nesub}$, $N_E^+ = \text{nesup}$, and $N_E = N_E^+ + N_E^- = \text{negrid}$ in the code input.

We also have another mode to evaluate the energy integral in the code called the ‘**egrid** mode’, whereas the above method is called the ‘**vgrid** mode’. In the **egrid** mode, the energy integral is calculated by the method suggested by Candy and Waltz [22], which is not exponentially accurate. We note, however, that if N_E is very small ($\lesssim 8$), we find empirically that the **egrid** mode may give better results than the **vgrid** mode. Therefore, the optimal choice of energy grid mode is governed by the simulation parameters.

Further discussion of our velocity-space coordinates can be found in [36].

3.2. Time integration

The gyrokinetic equation is symbolically denoted by

$$\frac{\partial g}{\partial t} = \mathcal{L}g + \mathcal{C}g + \mathcal{N}(g, g) \quad (30)$$

where \mathcal{L} is the linear term except the collision term, \mathcal{C} is the collision term which is also linear, and \mathcal{N} is the nonlinear term. We consider the time derivative using first-order finite differentiation for the linear term, treating the collision term by the implicit Euler method, and handling the nonlinear term explicitly by the third-order Adams–Bashforth method (AB3):

$$\frac{g^{n+1} - g^n}{\Delta t} = \mathcal{L}g^n r_t + \mathcal{L}g^{n+1}(1 - r_t) + \mathcal{C}g^{n+1} + \frac{23}{12}\mathcal{N}^n - \frac{4}{3}\mathcal{N}^{n-1} + \frac{5}{12}\mathcal{N}^{n-2} + \mathcal{O}(\Delta t) \quad (31)$$

where $\mathcal{N}^n = \mathcal{N}(g^n, g^n)$. The time-centering parameter r_t (`fexp` in the code input) may be chosen within the range $0 \leq r_t \leq 1$, where $r_t = 1$ ($r_t = 0$) represents a fully explicit (implicit) scheme. If $r_t \leq 1/2$, the scheme is stable for any Δt . We mainly use an implicit trapezoidal rule $r_t = 1/2$ which is second-order accurate and free from time step restrictions due to the linear term. Hereafter, we fix $r_t = 1/2$.

Note that Eq. (31) is linear with respect to g^{n+1} due to the explicitness of the nonlinear term. We then employ a Godunov splitting technique [37], which is first-order accurate in Δt , to separate the collision term:

$$\frac{g^{(*)} - g^n}{\Delta t} = \mathcal{L} \frac{g^n + g^{(*)}}{2} + \frac{23}{12}\mathcal{N}^n - \frac{4}{3}\mathcal{N}^{n-1} + \frac{5}{12}\mathcal{N}^{n-2}, \quad (32)$$

$$\frac{g^{n+1} - g^{(*)}}{\Delta t} = \mathcal{C}g^{n+1} + \mathcal{O}(\Delta t), \quad (33)$$

which greatly reduces the size of the matrix to be inverted. Solving for g^{n+1} , we obtain:

$$g^{n+1} = (1 - \Delta t \mathcal{C})^{-1} \left(1 - \frac{\Delta t}{2} \mathcal{L} \right)^{-1} \times \left[\left(1 + \frac{\Delta t}{2} \mathcal{L} \right) g^n + \Delta t \left(\frac{23}{12} \mathcal{N}^n - \frac{4}{3} \mathcal{N}^{n-1} + \frac{5}{12} \mathcal{N}^{n-2} \right) \right] + \mathcal{O}(\Delta t^2). \quad (34)$$

The method is first-order accurate in time. The use of AB3 for the nonlinear term is to make nonlinear runs stable. Note that the first time step for the nonlinear term is evaluated by the (explicit) Euler method (which is also first order in Δt), and the second timestep is evaluated using the second-order Adams–Bashforth scheme (AB2).

A second-order accurate method may, in principle, be derived by applying a higher-order scheme for the collision term as well, and by using a Strang splitting [38] for the operator splitting. The first two steps for the nonlinear term could also be computed using a higher-order method. These ideas are not implemented in the current version.

3.3. Gyrokinetic solver

We now describe the implicit advance of the linear terms in the gyrokinetic equation. Basically, the fields in the gyrokinetic equation can be obtained by a separate procedure, and the gyrokinetic equation becomes a differential equation with the given fields. Thus the collisionless gyrokinetic equation is written as

$$\frac{\partial g}{\partial t} + a_Z \frac{\partial g}{\partial Z} + a_0 g = \mathbf{b}_t \cdot \frac{\partial \Psi}{\partial t} + \mathbf{b}_Z \cdot \frac{\partial \Psi}{\partial Z} + \mathbf{b}_0 \cdot \Psi + S, \quad (35)$$

where $\Psi = (\phi, A_{\parallel}, \delta B_{\parallel})$, coefficients $a_{Z,0}$ and $\mathbf{b}_{t,Z,0}$ are functions of V_{\perp} and V_{\parallel} , and S contains the AB3 nonlinear term. The collision term is always consecutively applied after (35), but separately (Section 3.3.4).

We use a compact finite-difference method for evaluation of $\partial/\partial Z$ to achieve up to second-order accuracy with keeping the matrix bi-diagonal. To take into account global information, compact finite differencing schemes use the derivatives at neighboring grids to evaluate the derivatives. A general formula of the compact finite-difference scheme using two neighboring grids is

$$\frac{1}{2} \left((1 - r_Z) \frac{\partial g}{\partial Z} \Big|_i + (1 + r_Z) \frac{\partial g}{\partial Z} \Big|_{i+1} \right) = \frac{g_{i+1} - g_i}{\Delta Z} + \mathcal{O}(\Delta Z), \quad (36)$$

for $V_{\parallel} > 0$. (V_{\parallel} is a coefficient of $\partial g/\partial Z$. See (14).) Information at $i - 1$ instead of $i + 1$ should be used for $V_{\parallel} < 0$. (In the following discussions, we show equations for $V_{\parallel} > 0$ only.) $0 \leq r_Z \leq 1$ is the space-centering parameter specified by `bakdif` in the code. We fix $r_Z = 0$ in the following discussion, and therefore second-order accuracy is achieved.

Combining the trapezoidal rule for the time derivatives with the compact scheme for the space derivatives⁵

$$\begin{aligned} \frac{g_{i+\frac{1}{2}}^{n+1} - g_{i+\frac{1}{2}}^n}{\Delta t} + a_Z \frac{g_{i+1}^{n+\frac{1}{2}} - g_i^{n+\frac{1}{2}}}{\Delta Z} + a_0 g_{i+\frac{1}{2}}^{n+\frac{1}{2}} \\ = \mathbf{b}_t \cdot \frac{\Psi_{i+\frac{1}{2}}^{n+1} - \Psi_{i+\frac{1}{2}}^n}{\Delta t} + \mathbf{b}_Z \cdot \frac{\Psi_{i+1}^{n+\frac{1}{2}} - \Psi_i^{n+\frac{1}{2}}}{\Delta Z} + \mathbf{b}_0 \cdot \Psi_{i+\frac{1}{2}}^{n+\frac{1}{2}} + S_{i+\frac{1}{2}}^n \end{aligned} \quad (37)$$

where $i + 1/2$ denotes the average value of the variables at i and $i + 1$ grids, and similarly for $n + 1/2$. Then, the gyrokinetic equation is cast into the following symbolic form:

$$A_1 g_i^n + A_2 g_{i+1}^n + B_1 g_i^{n+1} + B_2 g_{i+1}^{n+1} = \mathbf{D}_1 \cdot \Psi_i^n + \mathbf{D}_2 \cdot \Psi_{i+1}^n + \mathbf{E}_1 \cdot \Psi_i^{n+1} + \mathbf{E}_2 \cdot \Psi_{i+1}^{n+1} + S_i^n + S_{i+1}^n. \quad (38)$$

⁵ The combination of the trapezoidal rule and the second-order compact finite differentiation was first suggested by Beam and Warming [39]. Note that the so-called Beam–Warming scheme refers to a different scheme.

3.3.1. Kotschenreuther's Green's function approach

Kotschenreuther et al. developed an efficient way to solve the gyrokinetic equation by breaking the large matrix to be inverted into a number of small matrices [18]. In the method, fields at the future timestep $n+1$ are obtained using a Green's function formalism to decouple parts of the matrix related to velocity-space integrations in the gyrokinetic equation. Consequently, the matrix to be inverted becomes $N_Z \times N_Z$ at each velocity grid for each species. (Due to the periodic boundary condition, $i = 0, N_Z$ modes are not independent.) The actual scheme [40] that was originally implemented in **GS2**, and has been inherited by **AstroGK**, differs slightly from that described in the original paper by Kotschenreuther et al., as described below.

Because (38) is linear with respect to variables at timestep $n+1$, the solution to the equation may consist of any linear combination of solutions to parts of the equation. Thus we may split the solution at timestep $n+1$ into two pieces, $g^{n+1} = g^{(\text{inh})} + g^{(\text{h})}$, each satisfying the following equations (here we ignore the spatial index i in the interest of clarity):

$$Ag^n + Bg^{(\text{inh})} = \mathbf{D} \cdot \Psi^n + \mathbf{E} \cdot \Psi^n + S^n, \quad (39)$$

$$Bg^{(\text{h})} = \mathbf{E} \cdot \Psi^{(*)}, \quad (40)$$

where $\Psi^{n+1} = \Psi^n + \Psi^{(*)}$. An inhomogeneous piece $g^{(\text{inh})}$ depends only on the known quantities at timestep n , thus is immediately solved, while a homogeneous piece $g^{(\text{h})}$ depends on the fields at timestep $n+1$. The unknown portion of the fields $\Psi^{(*)}$ may be solved as a separate step using a Green's function approach.

A formal homogeneous solution is given by

$$g^{(\text{h})} = B^{-1} \mathbf{E} \cdot \Psi^{(*)} = \left(\frac{\delta g}{\delta \phi} \right) \phi^{(*)} + \left(\frac{\delta g}{\delta A_{\parallel}} \right) A_{\parallel}^{(*)} + \left(\frac{\delta g}{\delta (\delta B_{\parallel})} \right) \delta B_{\parallel}^{(*)} \quad (41)$$

where $(\delta g / \delta \phi)$, $(\delta g / \delta A_{\parallel})$, and $(\delta g / \delta (\delta B_{\parallel}))$ are called the plasma response matrices. Using the response matrices, the field Eqs. (16)–(18) can be written as

$$\begin{pmatrix} P_{11} & P_{12} & P_{13} \\ P_{21} & P_{22} & P_{23} \\ P_{31} & P_{32} & P_{33} \end{pmatrix} \begin{pmatrix} \phi^{(*)} \\ A_{\parallel}^{(*)} \\ \delta B_{\parallel}^{(*)} \end{pmatrix} = \begin{pmatrix} Q_1 \\ Q_2 \\ Q_3 \end{pmatrix}, \quad (42)$$

where

$$P_{11} = \sum_s \left[q_s \mathcal{M}^{(0)} \left(\frac{\delta g_s}{\delta \phi} \right) - \frac{n_{0s} q_s^2}{T_{0s}} (1 - \Gamma_{0s}) I \right], \quad (43)$$

$$P_{12} = \sum_s q_s \mathcal{M}^{(0)} \left(\frac{\delta g_s}{\delta A_{\parallel}} \right), \quad (44)$$

$$P_{13} = \sum_s \left[q_s \mathcal{M}^{(0)} \left(\frac{\delta g_s}{\delta(\delta B_{\parallel})} \right) + q_s n_{0s} \Gamma_{1s} I \right], \quad (45)$$

$$P_{21} = \sum_s q_s n_{0s} \mathcal{M}^{(1)} \left(\frac{\delta g_s}{\delta \phi} \right), \quad (46)$$

$$P_{22} = -\frac{k_{\perp}^2}{2\beta_0} I + \sum_s q_s n_{0s} \mathcal{M}^{(1)} \left(\frac{\delta g_s}{\delta A_{\parallel}} \right), \quad (47)$$

$$P_{23} = \sum_s q_s n_{0s} \mathcal{M}^{(1)} \left(\frac{\delta g_s}{\delta(\delta B_{\parallel})} \right), \quad (48)$$

$$P_{31} = \sum_s \left[\mathcal{M}^{(2)} \left(\frac{\delta g_s}{\delta \phi} \right) + q_s n_{0s} \Gamma_{2s} I \right], \quad (49)$$

$$P_{32} = \sum_s \mathcal{M}^{(2)} \left(\frac{\delta g_s}{\delta A_{\parallel}} \right), \quad (50)$$

$$P_{33} = \frac{2}{\beta_0} I + \sum_s \left[\mathcal{M}^{(2)} \left(\frac{\delta g_s}{\delta(\delta B_{\parallel})} \right) + n_{0s} T_{0s} \Gamma_{2s} I \right], \quad (51)$$

with I being the $N_Z \times N_Z$ identity matrix and

$$Q_1 = \phi^n \sum_s \frac{n_{0s} q_s^2}{T_{0s}} (1 - \Gamma_{0s}) - \delta B_{\parallel}^n \sum_s q_s n_{0s} \Gamma_{1s} - \sum_s q_s \mathcal{M}^{(0)} \left(g_s^{(\text{inh})} \right), \quad (52)$$

$$Q_2 = \frac{k_{\perp}^2}{2\beta_0} A_{\parallel}^n - \sum_s q_s n_{0s} \mathcal{M}^{(1)} \left(g_s^{(\text{inh})} \right), \quad (53)$$

$$Q_3 = -\phi^n \sum_s q_s n_{0s} \Gamma_{1s} - \delta B_{\parallel}^n \left(\frac{2}{\beta_0} + \sum_s n_{0s} T_{0s} \Gamma_{2s} \right) - \mathcal{M}^{(2)} \left(g_s^{(\text{inh})} \right). \quad (54)$$

By solving the field Eq. (42), we obtain $\Psi^{(*)}$, and ultimately Ψ^{n+1} . Given Ψ^{n+1} , we solve (38) for g^{n+1} . This is equivalent to solving (39) with $\mathbf{E} \cdot \Psi^n$ replaced by $\mathbf{E} \cdot \Psi^{n+1}$. Finally, the full procedure to solve the gyrokinetic equation becomes:

1. Solve (39) and apply the collision term to obtain the inhomogeneous part of the distribution function $g^{(\text{inh})}$.
2. Solve (42) for $\Psi^{(*)}$, and obtain Ψ^{n+1} .
3. Replace $g^{(\text{inh})}$ by g^{n+1} and $\mathbf{E} \cdot \Psi^n$ by $\mathbf{E} \cdot \Psi^{n+1}$ in (39), solve it, and again apply the collision term to get g^{n+1} .

Up to this point in the subsection, we have ignored the i index for notational simplicity. In fact, the gyrokinetic equation and the field equations should be solved at all Z grids simultaneously. The field vector in (42) is actually a vector of length $N_f N_Z$, where N_f is the number of fields evolved. An electrostatic simulation requires only the evolution of ϕ and so has $N_f = 1$, whereas a fully electromagnetic simulation evolves ϕ , A_{\parallel} , and δB_{\parallel} and so has $N_f = 3$. Each of the elements of the P matrix in (42) represents an $N_Z \times N_Z$ matrix, so the entire P matrix is of size $(N_f N_Z) \times (N_f N_Z)$. Similarly, the Q vector is of length $N_f N_Z$.

To evaluate the computational efficiency of Kotschenreuther’s approach, let us compare it to a brute-force approach to solving the GK-M system. A brute-force approach requires the inversion of a dense $(N_Z N_\lambda N_E N_s)$ -size square matrix (where N_s is the number of species), which generally takes $\mathcal{O}\left((N_Z N_\lambda N_E N_s)^2\right)$ operations. On the other hand, Kotschenreuther’s method requires the following: (a) for the gyrokinetic equation, $(N_\lambda N_E N_s)$ inversions of bi-diagonal N_Z -size square matrices, which costs $\mathcal{O}(N_Z N_\lambda N_E N_s)$; and, (b) for the fields, the inversion of the matrix P in (42), a dense $(N_f N_Z)$ -size square matrix. For a fixed timestep Δt , however, the matrix P does not change, so this matrix inversion need only be performed once during an initialization stage. Therefore, during each timestep the field solver requires only an $\mathcal{O}\left((N_f N_Z)^2\right)$ matrix multiplication operation. Ignoring the factor N_f^2 since $N_f \leq 3$, Kotschenreuther’s approach requires $\mathcal{O}\left(N_Z^2 N_\lambda N_E N_s\right)$ operations per timestep, much more efficient than the brute-force approach.

3.3.2. Response matrix

A remaining task is to determine the response matrices, given in (41). For clarity, we rewrite (41) with the i index (in the code, the i index is counted from $-\text{ntgrid} + 1$ to ntgrid for $V_\parallel > 0$ with $2 \times \text{ntgrid} = N_Z$):

$$\begin{pmatrix} g_1^{(h)} \\ g_2^{(h)} \\ \vdots \\ g_{N_Z}^{(h)} \end{pmatrix} = B^{-1} \left[E_\phi \begin{pmatrix} \phi_1^{(*)} \\ \phi_2^{(*)} \\ \vdots \\ \phi_{N_Z}^{(*)} \end{pmatrix} + E_{A_\parallel} \begin{pmatrix} A_{\parallel,1}^{(*)} \\ A_{\parallel,2}^{(*)} \\ \vdots \\ A_{\parallel,N_Z}^{(*)} \end{pmatrix} + E_{\delta B_\parallel} \begin{pmatrix} \delta B_{\parallel,1}^{(*)} \\ \delta B_{\parallel,2}^{(*)} \\ \vdots \\ \delta B_{\parallel,N_Z}^{(*)} \end{pmatrix} \right], \quad (55)$$

where B and $E_{\phi, A_\parallel, \delta B_\parallel}$ are all $N_Z \times N_Z$ matrices. To obtain the response matrices $B^{-1} E_{\phi, A_\parallel, \delta B_\parallel}$, we solve (55) column by column. If we put trial functions $\check{\phi}_i = \delta_{il}$ (where δ_{il} is the Kronecker’s delta), $\check{A}_{\parallel,i} = 0$, $\check{\delta B}_{\parallel,i} = 0$ in the RHS of (55), a solution contains the l th column of $B^{-1} E_\phi$. By running l from 1 to N_Z , the full response matrix is calculated. The same procedures are carried out to obtain the other response matrices. This is fundamentally a Green’s function method.⁶ Note that we can use the same routine to get the response matrices as that to solve (38) by replacing $g^n = 0$, $\Psi^n = 0$, and Ψ^{n+1} with the trial functions.

3.3.3. Boundary conditions

The boundary condition in **AstroGK** in the Z direction is always periodic, thus it is rather trivial to implement the boundary condition compared with **GS2**. For the field equation, periodicity is immediately satisfied if the trial functions described in Section 3.3.2 satisfy periodicity. For the gyrokinetic equation, periodicity is imposed in the matrix B . Let us write the gyrokinetic equation as

$$B\mathbf{x} = \mathbf{y} \quad \text{where} \quad B = \begin{pmatrix} B_2 & 0 & \cdots & 0 & B_1 \\ B_1 & B_2 & \ddots & & 0 \\ 0 & B_1 & B_2 & \ddots & \vdots \\ \vdots & \ddots & \ddots & \ddots & 0 \\ 0 & \cdots & 0 & B_1 & B_2 \end{pmatrix}. \quad (56)$$

⁶The method can be trivially extended to Fourier space along Z when the coefficients of the linear terms are independent of Z . This may be advantageous for some applications but is not described here.

The matrix B is readily LU decomposed by forward elimination to yield:

$$B_2 \begin{pmatrix} 1 & 0 & \cdots & 0 & -\left(-\frac{B_1}{B_2}\right) \\ 0 & 1 & \ddots & \vdots & -\left(-\frac{B_1}{B_2}\right)^2 \\ & & \ddots & \ddots & \vdots \\ \vdots & & \ddots & \ddots & 0 \\ 0 & \cdots & 0 & 1 & -\left(-\frac{B_1}{B_2}\right)^{N_Z-1} \\ & & & & -\left(-\frac{B_1}{B_2}\right)^{N_Z} \end{pmatrix} \mathbf{x} = L^{-1}\mathbf{y}, \quad (57)$$

thus the equation is solved.

3.3.4. Collision term

The collision term is handled by operator splitting as shown in (33). After splitting, one must compute $(1 - \Delta t \mathcal{C})^{-1}$, where \mathcal{C} is an advanced model collision operator designed for gyrokinetics (Section 2 and Appendix B). The numerical implementation is given in [32]. Here we provide a brief overview of the key features.

The collision operator can be written schematically as

$$\mathcal{C} \equiv \mathcal{C}_L + \mathcal{C}_D + \mathcal{U}_L + \mathcal{U}_D, \quad (58)$$

where \mathcal{C}_L and \mathcal{C}_D are second-order differential operators describing pitch-angle scattering and energy diffusion, respectively, and \mathcal{U}_L and \mathcal{U}_D are integral operators designed to make \mathcal{C} conserve particle number, momentum, and energy. Since the collision operator includes velocity-space derivatives and integrals, but no coupling in Z , it consists of a dense $(N_\lambda N_E) \times (N_\lambda N_E)$ matrix.

Discretization and inversion of the operator $1 - \Delta t \mathcal{C}$ are done carefully to minimize computational expense and to preserve numerically the analytic conservation properties. First, we discretize the differential operators \mathcal{C}_L and \mathcal{C}_D on a three-point stencil using a novel discretization scheme that guarantees exact conservation properties on **AstroGK**'s nonuniform velocity-space grids. This is accomplished by incorporating the Gaussian integration weights in the discretization, leading to a first-order accurate scheme across most of the velocity-space domain.

Next, we apply another Godunov splitting so that we can invert two reduced matrices: $1 - \Delta t (\mathcal{C}_L + \mathcal{U}_L)$ and $1 - \Delta t (\mathcal{C}_D + \mathcal{U}_D)$. Both \mathcal{C}_L and \mathcal{C}_D can be written as tridiagonal matrices, but \mathcal{U}_L and \mathcal{U}_D are in general dense. However, both \mathcal{U}_L and \mathcal{U}_D can be expressed as tensor products, so that we can use the Sherman-Morrison formula [41, 42] to reduce greatly the numerical expense of the matrix inversions. Therefore, the inversion $(1 - \Delta t \mathcal{C})^{-1}$ is ultimately computed by inverting a small number of tridiagonal matrices.

3.4. Parallelization scheme

Decomposition of the gyrokinetic distribution function is accomplished using a flexible parallelization scheme that allows for several different memory layouts. In principle, the gyrokinetic distribution function is

$$g(k_x, k_y, Z, \lambda, E, \sigma, s), \quad (59)$$

comprising a scalar function defined on seven-dimensional discrete space. Since field quantities, ϕ , A_\parallel , and δB_\parallel , are three-dimensional and therefore have much smaller memory sizes than the distribution function, a copy of the full three-dimensional field information is held by each processor.⁷ Thus we focus on the parallelization scheme of the distribution function in this section.

⁷This can be a problem if we consider extremely large simulations. We may take a large number of processors N_{proc} , such that $N_{k_x} N_{k_y} N_\lambda N_E N_s / N_{\text{proc}} \ll N_{k_x} N_{k_y}$, as long as the work load on each processor is large enough to scale up computational efficiency. In such cases, data for the fields rather than the distribution function dominate memory usage.

The update of the distribution function using the gyrokinetic equation, as described in Section 3.3, is accomplished in several stages, including the main stage (Section 3.3.1), collision term stage (Section 3.3.4), and nonlinear term stage. Each of these stages performs operations over different dimensions of the seven-dimensional distribution function data. For example, the linear terms of the main stage involve compact finite differencing in Z ; the collision term employs velocity-space derivatives involving λ , σ , and E ; and the nonlinear term employs Fourier transforms requiring information along the components of the perpendicular wavenumber, k_x and k_y . We refer to the dimensions required for the current operation as the *active* dimensions, while the remaining dimensions are *inactive*.

The basic parallelization strategy is to place the seven-dimensional distribution function data into an array in memory such that the indices of the array associated with the active dimensions come first. Then all of the data associated with the inactive dimensions are combined into a single, final array index in the order specified by the variable `layout`. The data array is then decomposed across N_{proc} processors by splitting it up evenly over the final index containing all of the inactive dimensions. After one stage of the calculation is completed, the distribution function data is redistributed in preparation for the next stage of the calculation. This redistribution is accomplished by a series of one-to-one communications, carefully designed to perform only necessary communications and to avoid communication deadlocks. During the initialization for each run, the code determines this redistribution scheme.

For the gyrokinetic solver (Section 3.3), the redistribution of the seven-dimensional distribution function data into a three-dimensional data array is performed as follows. Since compact finite differences are used along the mean magnetic field (Z), the first index of the data array corresponds to the Z dimension. The second index is associated with σ since most operations are common to the same $|v_{\parallel}|$. The remaining five dimensions of the distribution function data are combined into the third index of the data array. The order of this combination may be chosen by the user to yield the best parallel performance by setting the character input variable `layout`, which consists of five alphabetical characters indicating the order of the dimensions. At present, the following options are available for `layout`: ‘`lxyes`’, ‘`lyxes`’, ‘`lexys`’, ‘`yxels`’, and ‘`yxles`’. For example, if `layout` = ‘`yxles`’, the data are combined into the final index such that k_y changes first, then k_x , then λ , then E , and finally s . Such a layout is advantageous, especially for collisionless simulations, when redistribution to calculate the collision term is unnecessary. If the number of processors N_{proc} is chosen such that all k_x and k_y indices are on the local processor [requiring $\text{mod}(N_{\lambda}N_EN_s, N_{\text{proc}}) = 0$], then redistribution for the nonlinear term is unnecessary.

For the nonlinear term, if the number of processors N_{proc} or the `layout` is chosen so that all k_x and k_y indices are not on the local processor, then the code redistributes the distribution function data over the processors into a two-dimensional data array with k_x (or k_y) as the first index and all remaining inactive dimensions into a second index to be split over processors. In this case, Z and σ are the first dimensions to be combined, and then remaining dimensions follow the layout specified in `layout`, except for k_x (or k_y). It then performs the one-dimensional fast Fourier transform in k_x (or k_y) to compute the nonlinear term. For the collision term, the code redistributes the data with λ and σ first to obtain the pitch angle ξ for the pitch-angle scattering term, and with E first for the energy diffusion term. Therefore, the more physics that is included in the calculation, the more redistribution that occurs, and the performance of the code diminishes as the complexity of the problem is increased. For large simulations employing $N_{\text{proc}} > 1000$, one must choose the number of processors and `layout` carefully to prevent the computational effort required for data redistribution from becoming a bottleneck.

3.5. Additional features

We list here some additional features implemented in `AstroGK` which have not yet been described.

3.5.1. Driven simulation

One might want to drive the system externally. For instance, turbulence simulation is quite often driven externally at large scale to achieve a driven-dissipative system where stationary turbulence inertial range spectrum will be observed.

In **AstroGK**, we can add $A_{\parallel}^{\text{antenna}}$ in (53) to drive an *antenna* current in the direction parallel to the mean magnetic field. In this case, the normalized parallel Ampère’s law (17) is modified as

$$\frac{k_{\perp}^2}{2\beta_0} \left(A_{\parallel, \mathbf{k}_{\perp}} + A_{\parallel, \mathbf{k}_{\perp}}^{\text{antenna}} \right) = \sum_s q_s n_{0s} \mathcal{M}^{(1)}(g_{\mathbf{k}_{\perp}, s}). \quad (60)$$

Property of the antenna is specified by its amplitude $A_{\parallel 0}$, frequency ω_0 , and wavenumber \mathbf{k}_0 :

$$A_{\parallel, \mathbf{k}_{\perp 0}}^{\text{antenna}} = A_{\parallel 0} e^{-i(\omega_0 t - \mathbf{k}_{\parallel 0} z)}. \quad (61)$$

3.5.2. Timestep

The timestep Δt is variable in **AstroGK**. For linear runs, the numerical scheme is unconditionally stable as long as $r_t \leq 1/2$, so adjustment of the timestep is necessary only to achieve an acceptable accuracy and does not affect the stability. For nonlinear runs, the nonlinear term is handled explicitly and therefore the code automatically adjusts the timestep to meet the CFL condition according to the nonlinear drift velocity in the plane perpendicular to the mean magnetic field.

We estimate an acceptable timestep based on the CFL condition as

$$\Delta t_{\text{CFL}} = C_{\text{CFL}} \min \left(\frac{\Delta x}{\max(v_{\text{D},x}^{\text{NL}})}, \frac{\Delta y}{\max(v_{\text{D},y}^{\text{NL}})} \right) \quad (62)$$

where the nonlinear drift velocity $\mathbf{v}_{\text{D}}^{\text{NL}}$ is given by the third term in (3), $\Delta x = 2\pi/k_{x,\text{max}}$, $\Delta y = 2\pi/k_{y,\text{max}}$, and C_{CFL} is a user input constant. We check if the current time step is greater than Δt_{CFL} at every timestep, and divide Δt by a constant factor (2 by default) if $\Delta t > \Delta t_{\text{CFL}}$. We also increase Δt by multiplying the same factor if Δt is substantially smaller than Δt_{CFL} .

If Δt changes, some matrices must be updated accordingly, so the initialization routine for the matrices is called at this timing. The first two steps for the nonlinear term after the timestep change are again the Euler method and AB2.

3.5.3. Diagnostics

AstroGK can write out the full data of the fields and the distribution functions. Frequent output of the full data is undesired due to the consumption of large amounts of disk space. Instead, the code computes reduced diagnostic data on the fly, including the following:

- Macroscopic quantities, such as the entropy, energies, heating rates, and certain averages of the fields and the moments [1, 28].
- Spectra in position and velocity spaces [27–29].
- Transfer functions of energies in position and velocity spaces [29].
- Linear frequency and growth rate [1, 31].
- Error estimate of velocity-space resolution [32, 36].

Some of the output utilize **NetCDF** or **HDF5** library to make structured binary data for portability.

4. Code verification

In this section, we provide some examples of **AstroGK** test runs, ranging from the simple linear, electrostatic ($A_{\parallel} = \delta B_{\parallel} = 0$) problems to fully nonlinear, electromagnetic problems. Validity of the linear physics within the code is demonstrated by the comparison of linear **AstroGK** results with analytic solutions. For nonlinear problems, comparison to an analytic solution is generally not simple, so here we compare with the nonlinear results of an independent reduced magnetohydrodynamics (MHD) code. In the large-scale limit $k_{\perp}\rho_i \ll 1$, the gyrokinetic-Maxwell equations simplify to the equations of reduced MHD [3], so such a comparison is useful to validate the nonlinear behavior of **AstroGK**. It is worth noting that the gyrokinetic simulations contain much richer physics and show interesting phenomena, but a detailed analysis of such behavior is beyond the scope of this paper and is left for future studies.

Unless otherwise stated, the plasma is assumed to be quasi-neutral with $n_{0i}/n_{0e} = -q_i/q_e = 1$. Free parameters are the ion-to-electron mass ratio m_i/m_e , the equilibrium ion-to-electron temperature ratio T_{0i}/T_{0e} , and the plasma beta β_s of the reference species s .

We comment on the number of grid points in the perpendicular plane of position space compared to the corresponding number of Fourier modes kept in the pseudo-spectral method. The number of grid points in the perpendicular plane N_x and N_y are specified by user. Dealiasing requires that Fourier modes must be discarded according to the 2/3 rule [43], giving the number of perpendicular wave modes in **AstroGK** $N_{k_x} \approx 2/3N_x$ and $N_{k_y} \approx 1/3N_y$. Note that the reality constraint on the complex Fourier coefficients means that the modes in the lower half ($k_y < 0$) of the (k_x, k_y) plane are not independent and need not be kept. In addition to the standard operating mode that nonlinearly evolves many Fourier modes, **AstroGK** also allows a very useful linear mode where $N_x = N_y = 1$ and only $|k_{\perp}|$ needs to be specified.

4.1. Linear physics of Alfvén waves

Testing the ability of **AstroGK** to model accurately the linear physics of Alfvén waves, including their dispersion and collisionless damping at sub-Larmor radius scales, is critical to demonstrating the validity of the code. The linear collisionless gyrokinetic dispersion relation [1] describes the physical behavior and provides analytical solutions for comparison to numerical results. It is worth noting here that the results of the linear collisionless gyrokinetic dispersion relation agree with the full Vlasov–Maxwell hot plasma dispersion relation [44] in the gyrokinetic limit, as has been demonstrated by Howes et al. [1].

The tests in this subsection explore the linear plasma response in a uniform plasma with a straight equilibrium magnetic field, so that $L_{B_0}^{-1} = L_{n_{0s}}^{-1} = L_{T_{0s}}^{-1} = \kappa = 0$. All tests use a realistic ion-to-electron mass ratio for protons, $m_i/m_e = 1836$. The linear frequencies and damping rates presented here are normalized by the MHD Alfvén frequency ω_A (defined later on), denoted by the overbar, $\bar{\omega} \equiv \omega/\omega_A$. With these simplifications, the normalized complex eigenfrequency of the linear collisionless gyrokinetic dispersion relation is a function of only three parameters, $\bar{\omega} = \bar{\omega}(k_{\perp}\rho_i, \beta_i, T_{0i}/T_{0e})$.

4.1.1. Linear Laplace–Fourier transform solution

Alfvén waves can be driven in **AstroGK** by applying a parallel antenna current throughout the simulation domain (see Section 3.5). The parallel vector potential due to the antenna drives a single wavevector $\mathbf{k}_0 = k_{\perp}\hat{\mathbf{x}} + k_{\parallel}\hat{\mathbf{z}}$ at a frequency ω_0 with amplitude $A_{\parallel 0}$. Using the parallel wave number of the drive, we can define the Alfvén frequency for the normalization as $\omega_A = k_{\parallel}v_A$, where the Alfvén velocity is defined by $v_A = B_0/\sqrt{\mu_0 n_{0i} m_i}$.

The amplitude response of the driven linear gyrokinetic system can be compared with an analytical Laplace–Fourier transform solution, given by (C.10) in Appendix C. For the example presented here, the parallel magnetic field perturbation was forced to be zero, $\delta B_{\parallel} = 0$. In Fig. 1, we plot the analytical Laplace–Fourier solution of the gyrokinetic system (solid line) and compare it to the output of **AstroGK** (dashed line). Parameters for the run are $k_{\perp}\rho_i = 1$, $\beta_i = 1$, and $T_{0i}/T_{0e} = 1$; the system is driven with amplitude $A_{\parallel 0} = 20$ (in arbitrary unit) at frequency $\bar{\omega}_0 = 0.9$ from zero initial conditions for the fields and perturbed distribution functions g_s . From the linear gyrokinetic dispersion relation, the linear eigenvalue for these parameters is $\bar{\omega} = \bar{\omega}_R + i\bar{\omega}_I = 1.4057 - 0.073004i$. The numbers of grids are $(N_Z, N_{\lambda}, N_E) = (32, 8, 32)$. These choices achieve a converged result with minimal computational effort. Low collision frequencies for the same-species

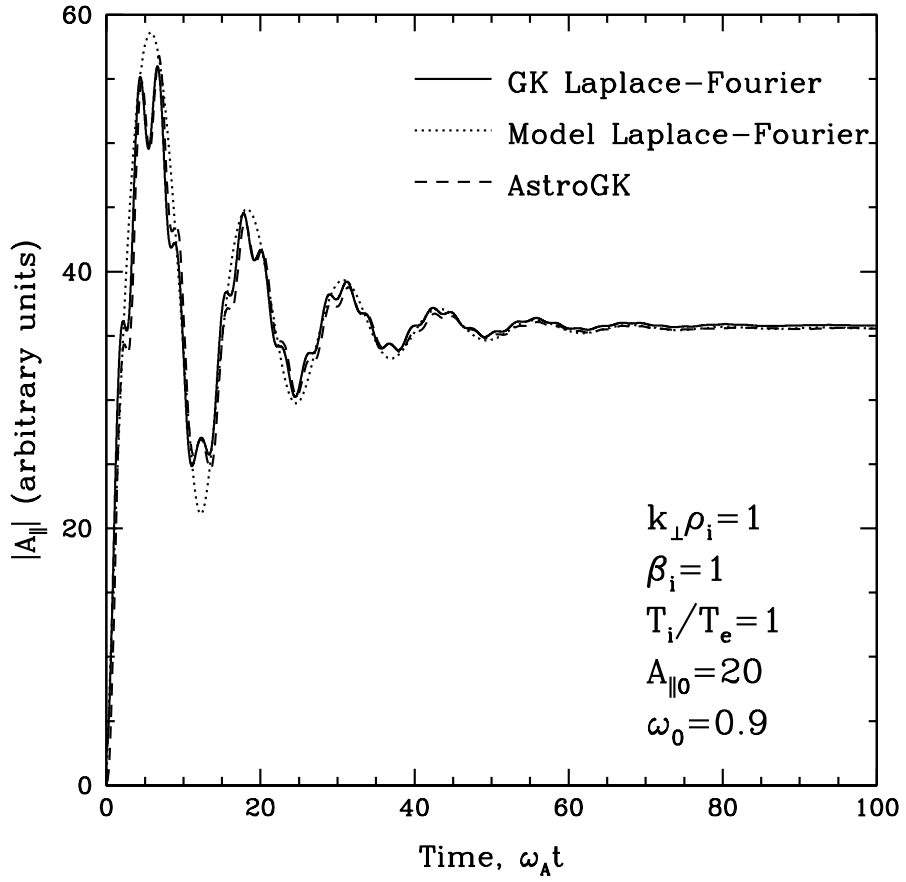


Figure 1: Evolution of the amplitude $|A_{\parallel}|$ vs. time from a linear AstroGK run (dashed line) with $\delta B_{\parallel} = 0$ for parameters $k_{\perp}\rho_i = 1$, $\beta_i = 1$, and $T_{0i}/T_{0e} = 1$. The Laplace-Fourier solutions of the gyrokinetic system (solid line) and a simple model system (dotted line) are given for comparison.

collisions are chosen to yield weakly collisional behavior, with $\nu_i/\omega_A = \nu_e/\omega_A = 2 \times 10^{-2}$. The close agreement of the solid and dashed lines in Fig. 1—faithfully reproducing even the small amplitude, high-frequency oscillation—demonstrates the ability of **AstroGK** to model accurately a driven linear gyrokinetic system.

To determine the effective frequency $\bar{\omega}_R$ and damping rate $-\bar{\omega}_I$ of the linear response to the driving in an **AstroGK** simulation, the Laplace–Fourier transform solution can be found for a model linear system. The model system treats the time evolution of A_{\parallel} as a linear operator with a complex eigenvalue given by $-i(\omega_R + i\omega_I)$ and includes the driving term,

$$\frac{\partial A_{\parallel}}{\partial t} = -i\omega A_{\parallel} + A_{\parallel 0} e^{-i\omega_0 t}. \quad (63)$$

The Laplace–Fourier transform solution yields the time evolution of the amplitude:

$$|A_{\parallel}(t)| = A_{\parallel 0} \left\{ \frac{1 + e^{2\omega_1 t} - 2e^{\omega_1 t} \cos[(\omega_R - \omega_0)t]}{(\omega_R - \omega_0)^2 + \omega_1^2} \right\}^{1/2}. \quad (64)$$

After normalizing frequencies appropriately, when $\bar{\omega}_0 = 0.9$, this function yields the fit (dotted line) in Fig. 1 with $A_{\parallel 0} = 18.2$ and $\bar{\omega} = 1.406 - 0.073i$. Note that fitting the oscillation of the solution at the beat frequency $(\omega_R - \omega_0)$ allows a precise determination of the resonant frequency. The fractional error in the damping rate is larger, in particular due to the difficulty of fitting the exponential decay in the presence of the higher frequency oscillations arising in the gyrokinetic system—compare the difference between the simple model (dotted line) and the gyrokinetic solution (solid line). Estimating the error in the frequency and damping rate based on these fits, we determine values of $\bar{\omega}_R = 1.406 \pm 0.004$ and $-\bar{\omega}_I = 0.073 \pm 0.003$.

4.1.2. Linear frequencies and damping rates

The model Laplace–Fourier transform solution given by (64) is used to determine the normalized frequencies ($\bar{\omega}_R$) and damping rates ($-\bar{\omega}_I$) of linear modes on the Alfvén branch, including the kinetic Alfvén wave at $k_{\perp}\rho_i \gg 1$, over a wide range of plasma parameters. In the upper panels of Fig. 2, we present the normalized (a) frequencies and (b) damping rates of the Alfvén solution vs. perpendicular wavenumber $k_{\perp}\rho_i$ for varied values of ion plasma beta $\beta_i = 0.01, 1, 100$ at $T_{0i}/T_{0e} = 1$; in the lower panels are the normalized (c) frequencies and (d) damping rates of the Alfvén solution for varied values of ion-to-electron temperature ratio $T_{0i}/T_{0e} = 0.2, 1, 100$ with $\beta_i = 1$. The numbers of grids are $(N_Z, N_{\lambda}, N_E) = (32, 8, 32)$. To ensure that structure in velocity space does not reach the velocity grid Nyquist frequency, the same species collisionalities are set in the range to $0.1|\omega_{I,s}| \lesssim \nu_s \lesssim |\omega_{I,s}|$ for each run.

4.1.3. Linear ion-to-electron heating ratios

Using the heating equations for gyrokinetics [1], we calculate the ion-to-electron heating ratio P_i/P_e from the linear collisionless gyrokinetic dispersion relation and compare it to the results of **AstroGK**. The results are presented in Fig. 3 for parameters $\beta_i = 10$ and $T_{0i}/T_{0e} = 100$, chosen to give the heating ratio that varies by many orders of magnitude around $k_{\perp}\rho_i \sim 1$. The resolution for these runs is $(N_Z, N_{\lambda}, N_E) = (64, 64, 32)$. The results of **AstroGK** show excellent agreement with theory over seven orders of magnitude in P_i/P_e .

4.2. Linear Ion-Temperature-Gradient (ITG) instability

Here we describe linear drift-wave dynamics in the collisionless limit [45, 46] to validate the electrostatic calculation of **AstroGK** with a Boltzmann electron response. We assume $L_{B_0}^{-1} = \kappa = L_{n_{0s}}^{-1} = 0$. Considering an ion distribution function with $\exp[i(\mathbf{k} \cdot \mathbf{r} - \omega t)]$ dependence, from (2) we find:

$$h_{\mathbf{k}_{\perp}, i} = \frac{q_i \phi_{\mathbf{k}_{\perp}}}{T_{0i}} \frac{\omega}{\omega - k_{\parallel} V_{\parallel}} \left[1 + \frac{\omega_{*T}}{\omega} \left(\frac{V^2}{v_{\text{th}, i}^2} - \frac{3}{2} \right) \right] J_0(\alpha_i) f_{0i}, \quad (65)$$

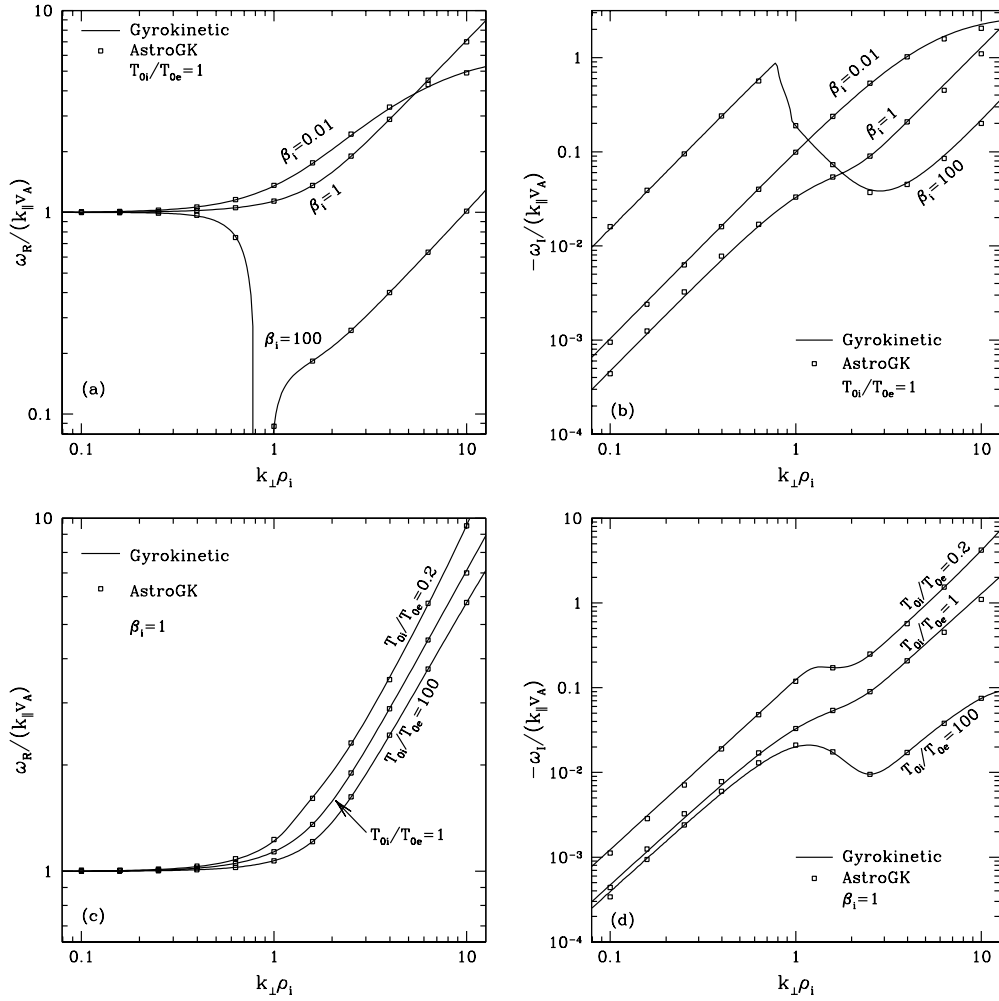


Figure 2: The normalized (a and c) real frequency $\bar{\omega}_R = \omega_R/\omega_A$ and (b and d) damping rate $-\bar{\omega}_I = -\omega_I/\omega_A$ vs. $k_{\perp}\rho_i$ for varied ion plasma beta $\beta_i = 0.01, 1, 100$ with fixed $T_{0i}/T_{0e} = 1$ (a and b) and for varied ion-to-electron temperature ratio $T_{0i}/T_{0e} = 0.2, 1, 100$ with fixed $\beta_i = 1$ (c and d) from the gyrokinetic dispersion relation (solid line) and linear AstroGK simulations (open squares).

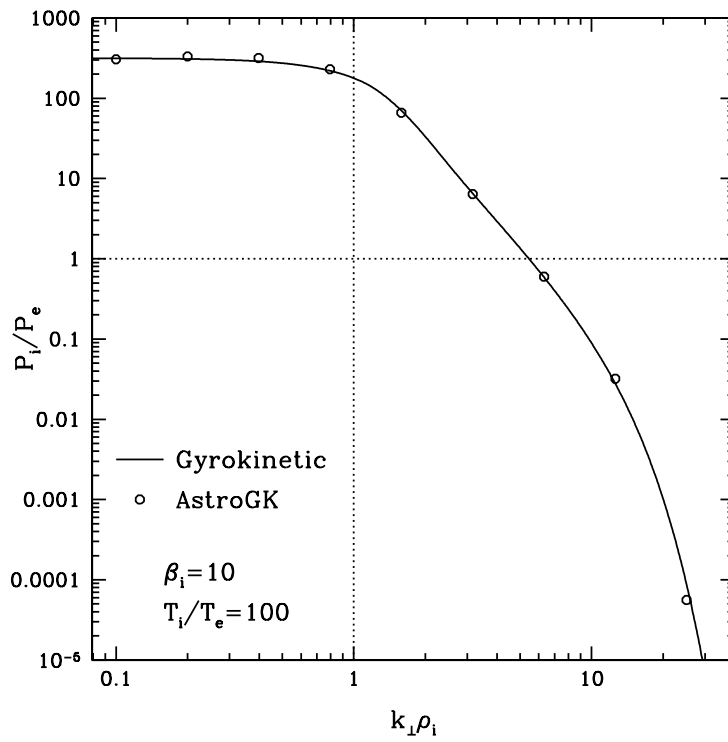


Figure 3: Ratio of the ion-to-electron heating P_i/P_e . Results are shown for $\beta_i = 10$ and $T_{0i}/T_{0e} = 100$. The analytical results from the linear collisionless gyrokinetic dispersion relation (solid line) are compared to **AstroGK** results (circles), showing excellent agreement over seven orders of magnitude in P_i/P_e .

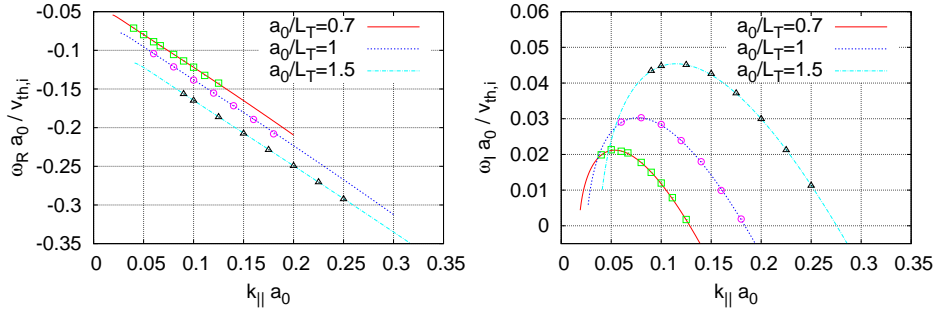


Figure 4: Dispersion relation of the slab ITG instability under the code normalization (see Appendix A.2). Left: frequency (ω_R), Right: growth rate (ω_I). Lines are from dispersion relation (67) and symbols are from **AstroGK**.

where we have introduced the drift frequency:

$$\omega_{*T} = \frac{1}{2} \frac{k_y \rho_i v_{th,i}}{L_{T_{0i}}} = \frac{k_y T_{0i}}{L_{T_{0i}} q_i B_0}. \quad (66)$$

Plugging this into the quasi-neutrality condition with the Boltzmann electron response $h_e = 0$, we obtain the following dispersion relation:

$$\frac{q_e^2 n_{0e}}{T_{0e}} + \frac{q_i^2 n_{0i}}{T_{0i}} = -\frac{q_i^2 n_{0i}}{T_{0i}} \Gamma_{0i} \zeta_i \Xi(\zeta_i) + \frac{q_i^2 n_{0i}}{T_{0i}} \frac{\omega_{*T}}{\omega} \left[\left(\frac{1}{2} \Gamma_{0i} + b_i \Gamma_{1i} \right) \zeta_i \Xi(\zeta_i) - \zeta_i^2 \Gamma_{0i} (1 + \zeta_i \Xi(\zeta_i)) \right], \quad (67)$$

where $\zeta_i = \omega / (k_{\parallel} v_{th,i})$, and Ξ is the plasma dispersion function [47].

We excite a perturbation of $h_i \propto f_{0i}$ which generates an electrostatic potential perturbation. A_{\parallel} and δB_{\parallel} are forced to be zero throughout the simulation. For the following parameters, $T_{0i}/T_{0e} = 1$, $(k_x \rho_i, k_y \rho_i) = (0, 1)$, the numerical solution to the dispersion relation (67) and the eigenvalues ω obtained from **AstroGK** are shown in Fig. 4. We take $(N_Z, N_{\lambda}, N_E) = (32, 16, 16)$ for all runs. The figure shows perfect agreement between the numerical solution and the theory, even though reproducing a slowly growing mode with small k_{\parallel} is particularly challenging since **AstroGK** uses a finite-difference scheme in the Z direction.

4.3. Collisions and velocity-space resolution

Here we demonstrate the accuracy of the collision model employed in **AstroGK** and the spectral convergence of the velocity-space integration. For the convergence studies, we again consider the electrostatic plasma slab with a background ion temperature gradient and a Boltzmann response for the electrons. We focus on the case with $T_{0i}/T_{0e} = k_{\parallel} L_{T_{0i}} = k_{\perp} \rho_i = 1$, and we use $(N_Z, N_{\lambda}, N_E) = (256, 128, 256)$ as our base case resolution. We then independently vary N_E and N_{λ} and calculate the relative error in the ITG mode frequency and growth rate.

Results from the convergence study are given in Fig. 5. The relative error, ϵ , is defined as

$$\epsilon = \frac{|\omega_{\text{agk}} - \omega|}{|\omega|}, \quad (68)$$

where ω_{agk} is the complex frequency computed in **AstroGK** and ω is the analytic frequency. We see that ϵ (dashed line) is less than 1% for $N_E \gtrsim 10$ and $N_{\lambda} \gtrsim 3$. Also, the relative error exhibits the exponential convergence indicative of a spectrally accurate discretization scheme. Accuracy at large number of velocity-space grid points is limited only by computational precision, as we see for $N_{\lambda} = 64$ (double precision is used here).

Also shown in Fig. 5 is an error estimate calculated on the fly as a velocity-space resolution diagnostic in **AstroGK** (solid line). A detailed description of the diagnostic is given in [36]. The basic idea is to calculate the fields using both the standard velocity-space integration scheme and a less accurate integration

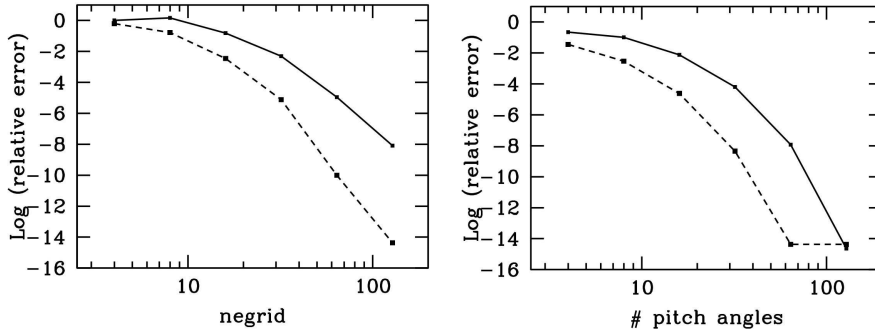


Figure 5: Error estimates in ITG frequency and growth rate as the number of velocity-space grid points is varied. Left: N_E dependence, Right: the number of pitch angles ($=2N_\lambda$) dependence. The solid line is obtained from the `AstroGK` velocity-space error diagnostics described in the text, and the dashed line is the relative error given by (68). The error decreases faster than a power law, a result of the spectral accuracy of the velocity-space integration.

scheme that involves dropping a velocity-space grid point and recalculating integration weights. By using the reduced grid and corresponding weights, the spectral accuracy is lost. Consequently, the error estimate is quite conservative: it is essentially computing the error for a simulation with half the order of accuracy (similar to using half as many grid points). In fact, we see in Fig. 5 that the error estimate agrees rather well with the actual error at half the number of grid points. The qualitative trend is correct, but one must realize that the quantitative error estimate is conservative.

4.3.1. Slow mode damping

For the collision operator verification, we consider slow mode damping in the low $k_\perp \rho_i$, high β_i limit. Here, analytic expressions can be obtained in both the strongly collisional ($k_\parallel \lambda_{\text{mfp}} \ll 1$) and collisionless ($k_\parallel \lambda_{\text{mfp}} \gg 1$) regimes, where $\lambda_{\text{mfp}} = v_{\text{th},i}/\nu_i$ is the ion mean free path. The complex frequencies are given by

$$\omega = -i \frac{|k_\parallel| v_A}{\sqrt{\pi} \beta_i} \quad (69)$$

for $k_\parallel \lambda_{\text{mfp}} \gg 1$, and

$$\omega = \pm k_\parallel v_A \sqrt{1 - \left(\frac{\mu_{\parallel,i} k_\parallel}{2v_A}\right)^2} - i \frac{\mu_{\parallel,i} k_\parallel^2}{2} \quad (70)$$

for $k_\parallel \lambda_{\text{mfp}} \ll 1$, with $\mu_{\parallel,i} \propto v_{\text{th},i} \lambda_{\text{mfp}}$ being the parallel ion viscosity. From these expressions, we see that the damping in the strongly collisional regime (70) is due primarily to viscosity, while the collisionless regime (69) is dominated by Barnes damping.

In order to isolate the slow mode from the Alfvén wave, we take $\phi = A_\parallel = 0$ throughout the simulation. The electron dynamics can be neglected because of the high β_i . Consequently, the system is described by the ion dynamics coupled with the δB_\parallel fluctuation (see Section 6 in [3]). We initially launch a perturbation of the form, $\delta f_i \propto (V_\perp^2/v_{\text{th},i}^2 - 1)f_{0i}$, which generates δB_\parallel perturbation, and measure the damping rate of δB_\parallel .

In Fig. 6, we plot the collisional dependence of the numerically obtained slow mode damping rate for $k_\perp \rho_i = 10^{-5}$, $\beta_i = 100$. For the most collisionless case which requires the highest resolution in velocity space, we take $(N_Z, N_\lambda, N_E) = (32, 32, 64)$. We find quantitative agreement with the analytic expressions (69) and (70) in the appropriate regimes. In particular, we recover the correct viscous behavior in the $k_\parallel \lambda_{\text{mfp}} \ll 1$ limit (damping rate proportional to $\mu_{\parallel,i}$), the correct collisional damping in the $k_\parallel \lambda_{\text{mfp}} \sim 1$ limit (damping rate inversely proportional to $\mu_{\parallel,i}$), and the correct collisionless (i.e. Barnes) damping in the $k_\parallel \lambda_{\text{mfp}} \gg 1$ limit. The proportionality constant $c \equiv \mu_{\parallel,i}/(v_{\text{th},i} \lambda_{\text{mfp}})$ estimated from the simulation is $c \approx 2.5$, while $c \approx 0.9$ from the Braginskii's analysis [48].

Slow Mode Damping

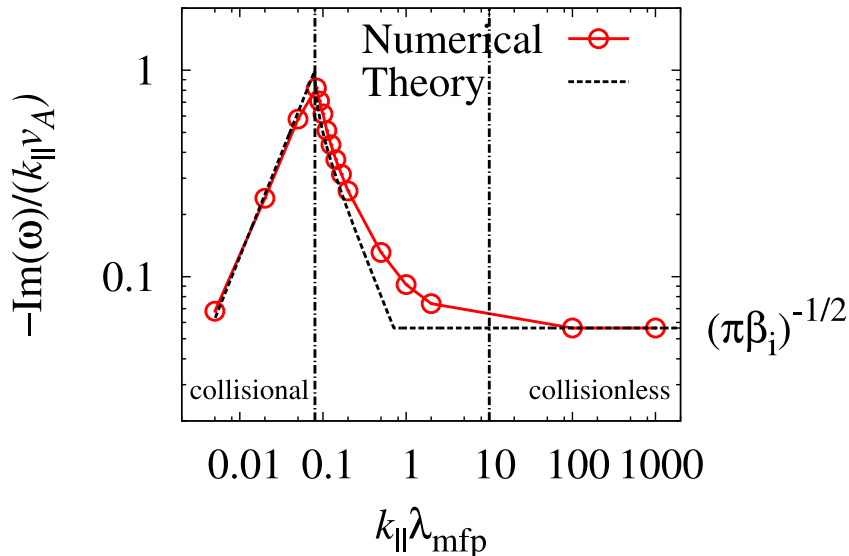


Figure 6: Damping rate of the slow mode for a range of collisionalities spanning the collisionless to strongly collisional regimes. Dashed lines correspond to the theoretical prediction for the damping rate in the collisional ($k_{\parallel} \lambda_{\text{mfp}} \ll 1$) and collisionless ($k_{\parallel} \lambda_{\text{mfp}} \gg 1$) limits. The ion parallel viscosity is estimated by fitting numerical data with the theory as $\mu_{\parallel,i} \approx 2.5 v_{\text{th},i} \lambda_{\text{mfp}}$. The solid line is the result obtained numerically with **AstroGK**. Vertical dot-dashed lines denote approximate regions (collisional and collisionless) for which the analytic theory is valid.

4.4. Linear tearing instability

A tearing instability [49] is one kind of magnetic reconnection process driven by the free magnetic energy stored in the current sheet configuration, and is a fascinating example to study in the gyrokinetic framework.

In collisional plasmas, inter-species collisions producing the resistivity allow topological changes of the magnetic field lines. The singularity occurs around the magnetic neutral line in the ideal limit, which is regularized by the finite resistivity. This is a standard boundary layer problem. The growth rate and boundary layer width scalings with respect to the Lundquist number S are obtained in [49].

As the collisionality is decreased, the boundary layer becomes narrower until kinetic effects come into play, such as the Hall effect (ion inertia), FLR effects, and electron inertial effects. Therefore, the scaling law should be altered in such weakly collisional plasmas. In most situations of interest in fusion and astrophysical plasmas, these effects can play a crucial role in the problem.

AstroGK includes full collision physics, and therefore correctly captures the macroscopic resistivity. (The resistivity is given by $\eta \approx 0.38 \mu_0 \nu_e d_e^2$, where ν_e is the electron collision frequency and d_e is the electron skin depth [50].) We provide here a scaling study of the problem in purely two-dimensional setting ($\partial/\partial Z = 0$) as the collisionality is varied, effectively varying the Lundquist number S . We consider an equilibrium distribution function of electrons as a shifted Maxwellian $\delta f_e \propto V_{\parallel} f_{0e}$ to give the following current sheet configuration:

$$A_{\parallel}^{\text{eq}} = A_{\parallel 0}^{\text{eq}} \cosh^{-2} \left(\frac{x - L_x/2}{a} \right) S_{\text{h}}(x) \quad (71)$$

where

$$S_{\text{h}}(x) = \frac{\tanh^2 \left(\frac{2\pi}{L_x} x \right) + \tanh^2 \left(\frac{2\pi}{L_x} x - 2\pi \right) - \tanh^2(2\pi)}{2 \tanh^2 \pi - \tanh^2(2\pi)}$$

is a shape function to ensure periodicity in the box sized $L_x = 3.2\pi a$, $A_{\parallel 0}^{\text{eq}}$ is a constant. We take $a = 50\rho_i$ so that the kinetic effect is relatively weak. We perturb the system with $k_y a = 0.8$ ⁸ (giving a standard stability index [49] $\Delta' a \approx 23.2$), and observe the linear growth rate. We fix $(N_\lambda, N_E) = (20, 16)$, and N_x varies from 512 to 2048 to resolve the current layer.

Figure 7 shows the scaling of the growth rate and current layer width as the Lundquist number S is increased. The Lundquist number is defined by $S = \mu_0 a v_{A\perp} / \eta = 2.63(\nu_e \tau_A)^{-1} (d_e/a)^{-2}$ with $\tau_A = a/v_{A\perp}$, so increased Lundquist number corresponds to decreased electron collisionality ν_e . The growth rate is normalized by the standard MHD time scale τ_A . The Alfvén velocity $v_{A\perp}$ is measured by the peak value of the background magnetic field given by (71).

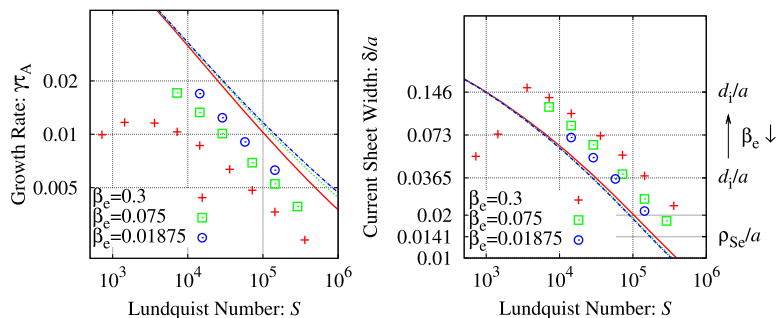


Figure 7: (Color online) Normalized growth rate (left) and current layer width (right) scaling against the Lundquist number S . Those obtained from **AstroGK** (symbols) and from the two-fluid model (lines) are shown for three sets of $(\beta_e, m_i/m_e)$.

For a fixed value of $T_{0i}/T_{0e} = 1$, we evaluate the Lundquist number dependence for three sets of parameters: $(\beta_e, m_i/m_e) = (0.3, 100)$, $(0.075, 400)$, and $(0.01875, 1600)$. For the given parameters, the characteristic scale lengths of the kinetic effects are the ion sound Larmor radius $\rho_{Se} \equiv \sqrt{T_{0e}/m_i}/\Omega_i = 0.0141a$, and the ion inertial skin depth $d_i/a = 0.365, 0.73, 0.146$. We also show the scaling obtained from the two-fluid MHD model by Fitzpatrick and Porcelli [51] for reference. For the given parameters, the two-fluid scaling is almost equal to that from the single-fluid model.

For the small β_e case, we observe that the gyrokinetic scaling is close to that from the fluid model as expected. However, as β_e is increased, the scaling deviates and the growth rate decreases as kinetic effects become non-negligible. The major difference between the two-fluid model and the kinetic simulation using **AstroGK** originates from the treatment of the second-order velocity moment (temperature or pressure). The fluid model assumes adiabatic ions and isothermal electrons, whereas the gyrokinetic pressure is generally tensorial and thus contains far richer physics [30].

4.5. Orszag–Tang vortex problem

To validate that results of **AstroGK** for a nonlinear electromagnetic problem, we present here the well-known MHD vortex problem of Orszag and Tang [52]. Their original simulation solves incompressible reduced MHD equations for the stream function φ ($= -\phi/B_0$) and flux function ψ ($= A_{\parallel}$) defined in the

⁸ The initial distribution function of electrons in total becomes:

$$\delta f_e = \frac{q_e}{T_{0e}} V_{\parallel} f_{0e} \sum_{\mathbf{k}} (k_{\perp} d_e)^2 (A_{\parallel, \mathbf{k}}^{\text{eq}} + \epsilon A_{\parallel 0}^{\text{eq}} \delta(k_x a = 0, k_y a = 0.8)) e^{k_{\perp}^2 \rho_e^2 / 4} e^{i\mathbf{k}_{\perp} \cdot \mathbf{R}_e}, \quad (72)$$

where $A_{\parallel, \mathbf{k}}^{\text{eq}}$ is a Fourier representation of (71), the second term gives a small sinusoidal perturbation with ϵ being a small constant, and δ is the Dirac’s delta function.

plane perpendicular to the mean magnetic field:

$$\frac{\partial}{\partial t} \nabla_{\perp}^2 \varphi + \{\varphi, \nabla_{\perp}^2 \varphi\} = \frac{1}{\mu_0 n_{0i} m_i} \{\psi, \nabla_{\perp}^2 \psi\} + \frac{\mu}{n_{0i} m_i} \nabla_{\perp}^4 \varphi, \quad (73)$$

$$\frac{\partial}{\partial t} \psi + \{\varphi, \psi\} = \frac{\eta}{\mu_0} \nabla_{\perp}^2 \psi, \quad (74)$$

where μ and η are the viscosity and resistivity. The nonlinear evolution of a system governed by the reduced MHD equations provides a useful comparison for the nonlinear evolution of the GK-M equations using **AstroGK**. Since GK-M equations in the large-scale limit, $k_{\perp} \rho_i \ll 1$, simplify to the equations of reduced MHD [3], the results of **AstroGK** in this limit should be similar to the results of a reduced MHD code, which does not contain the small scale physics that occurs when $k_{\perp} \rho_i \gtrsim 1$.

Given an initial condition:

$$\varphi = -2av_{A\perp} \left(\cos 2\pi \frac{x}{L_x} + \cos 2\pi \frac{y}{L_y} \right), \quad (75)$$

$$\psi = aB_{\perp 0} \left(\cos 4\pi \frac{x}{L_x} + 2 \cos 2\pi \frac{y}{L_y} \right), \quad (76)$$

where $v_{A\perp} = B_{\perp 0} / \sqrt{\mu_0 n_{0i} m_i}$ and $L_x = L_y = 2\pi a$, we have made a simulation of the initial value problem using an independent reduced MHD code. The initial conditions clearly define the standard MHD units for normalization: namely, system size a and Alfvén transit time $\tau_A = a/v_{A\perp}$. The dimensionless dissipation parameters are the Reynolds number $R_e \equiv av_{A\perp} n_0 m_i / \mu$ and the Lundquist number $S \equiv \mu_0 av_{A\perp} / \eta$. We use $(N_x, N_y) = (256, 256)$ grid points with the dissipation coefficients $1/R_e = 1/S = 1.5 \times 10^{-3}$.

For the **AstroGK** simulation, we set initial conditions on the distribution function for each species h_s to give the corresponding fields. Therefore, we define the distribution functions by

$$h_i = C_{\phi} \left(\cos 2\pi \frac{x}{L_x} + \cos 2\pi \frac{y}{L_y} \right) f_{0i}, \quad (77)$$

$$h_e = C_{A_{\parallel}} \left(2 \cos 4\pi \frac{x}{L_x} + \cos 2\pi \frac{y}{L_y} \right) V_{\parallel} f_{0e}, \quad (78)$$

where C_{ϕ} and $C_{A_{\parallel}}$ are coefficients chosen such that the resulting ϕ and A_{\parallel} are equivalent to (75) and (76). We use $(N_x, N_y, N_{\lambda}, N_E) = (256, 256, 32, 16)$ points, $T_{0i}/T_{0e} = 1$, $m_i/m_e = 1836$, $\beta_i = 10^{-3}$, $\rho_i/a = 0.01$, and ignore collisions. We assume $\delta B_{\parallel} = 0$.

Time evolutions of various energies are shown in Fig. 8 for both codes. Time and the energy are normalized to the MHD units, i.e. τ_A and $B_{\perp 0}^2 / \mu_0$. The result from **AstroGK** simulation also shows the gyrokinetic energy:

$$\begin{aligned} E_{\text{GK}} &= L_x L_y \sum_{\mathbf{k}_{\perp}} \left[\sum_s \int \frac{T_{0s} |h_{s, \mathbf{k}_{\perp}}|^2}{2f_{0s}} d\mathbf{v} - \left(\sum_s \frac{q_s^2 n_{0s}}{2T_{0s}} \right) |\phi_{\mathbf{k}_{\perp}}|^2 + \frac{k_{\perp}^2 |A_{\parallel, \mathbf{k}_{\perp}}|^2}{2\mu_0} \right] \\ &= L_x L_y \sum_{\mathbf{k}_{\perp}} \left[\sum_s \int \frac{T_{0s} |g_{s, \mathbf{k}_{\perp}}|^2}{2f_{0s}} d\mathbf{v} + \left(\sum_s \frac{q_s^2 n_{0s}}{2T_{0s}} \right) (1 - \Gamma_{0s}) |\phi_{\mathbf{k}_{\perp}}|^2 + \frac{k_{\perp}^2 |A_{\parallel, \mathbf{k}_{\perp}}|^2}{2\mu_0} \right], \end{aligned} \quad (79)$$

normalized into the MHD units. The kinetic energy ($E_K = L_x L_y \sum_{\mathbf{k}_{\perp}} (n_{0i} m_i / 2) |k_{\perp} \varphi_{\mathbf{k}_{\perp}}|^2$) and magnetic energy ($E_M = L_x L_y \sum_{\mathbf{k}_{\perp}} |k_{\perp} \psi_{\mathbf{k}_{\perp}}|^2 / (2\mu_0)$) evolve similarly in the two models. It is noted that the leading contribution of the ion part of the second term in (79) yields the kinetic energy. Thus the difference between the gyrokinetic energy E_{GK} and the MHD energy $E_{\text{MHD}} = E_K + E_M$ comes from g_s^2 and the electron part of the second term in (79). The apparent agreement of E_{GK} and E_{MHD} in the initial phase is not strange since the energy contained in the fields is much bigger than that in g by a factor of β_i^{-1} . This is true for the Alfvénic dynamics—the pure linear Alfvén wave propagates with approximately zero g [3].

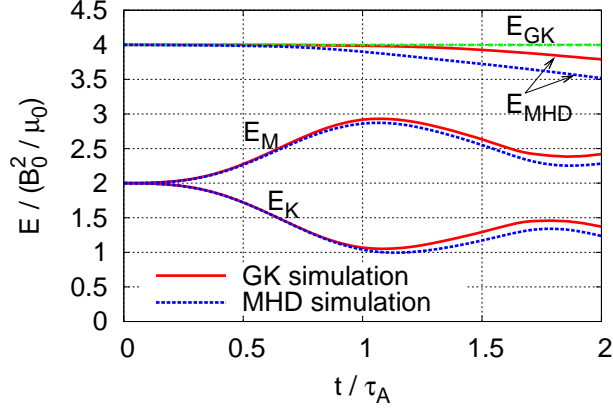


Figure 8: Time evolution of various energies. Red solid lines represent values from *AstroGK* and blue dashed from reduced MHD simulations. Note that E_{GK} is only defined for *AstroGK* simulation.

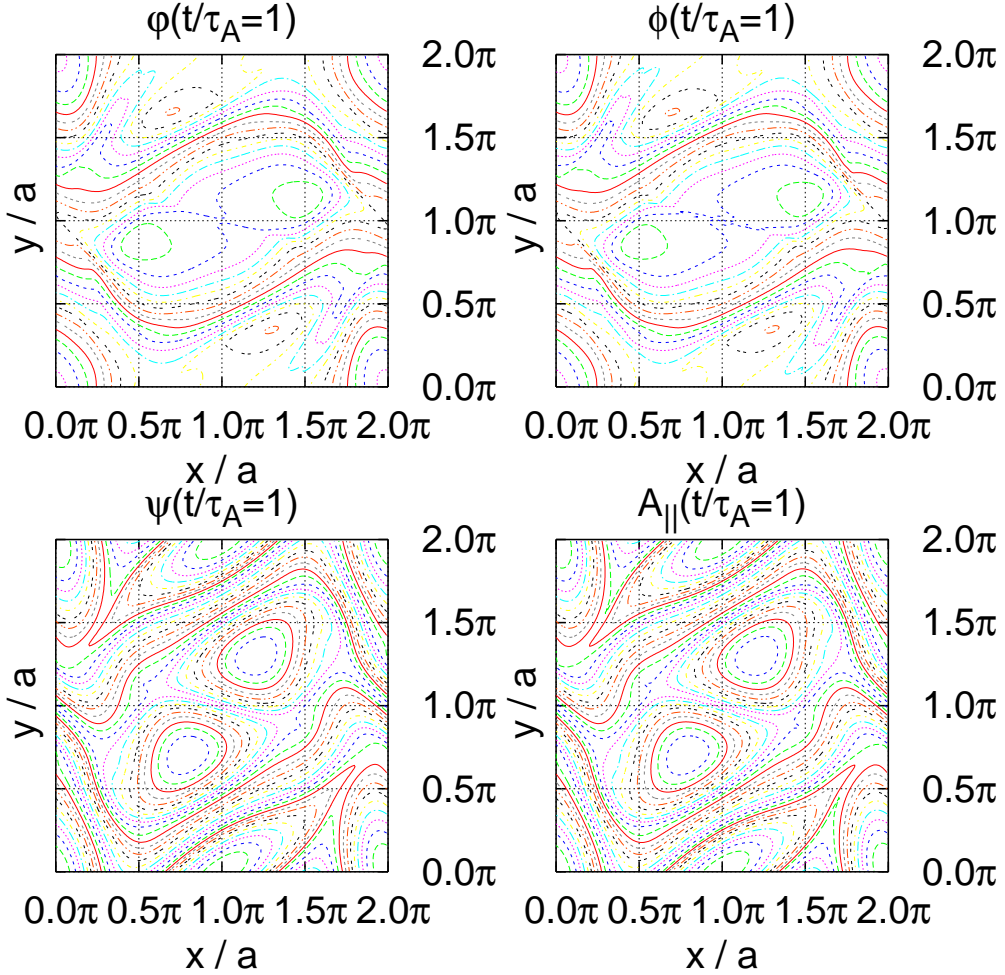


Figure 9: Stream and flux functions at $t/\tau_A = 1$ taken from reduced MHD (left) and *AstroGK* (right) simulations.

Contour plots of the stream and flux functions are also shown in Fig. 9. The overall agreement is almost perfect, which implies that **AstroGK** correctly reproduces MHD results. The small differences in these plots, especially at the small scales, are due to the kinetic effects resolved by **AstroGK** and are therefore physically meaningful. A more thorough discussion of these differences will be discussed elsewhere.

5. Performance

In this section, we determine the scaling of **AstroGK** with each of the problem dimensions and evaluate the strong and weak scalings of the parallel performance. The scaling performance tests in this section employ a nonlinear simulation of driven turbulence with plasma parameters $\beta_i = T_{0i}/T_{0e} = n_{0i}/n_{0e} = -q_i/q_e = 1$, $m_i/m_e = 1836$. The simulation is stirred by an antenna at the smallest wavenumber in the box corresponding to $k_{\perp}\rho_i = 1$ and collisions are turned off.

5.1. Single processor scaling with problem dimensions

We can determine the scaling of the time per step in **AstroGK** as each of the dimensions of the problem is increased. These tests are performed on a single processor to eliminate the requirement for communications between processors. We begin with a small nonlinear run with the following problem dimensions: $(N_x, N_y, N_Z, N_{\lambda}, N_E, N_s) = (4, 4, 8, 4, 2, 2)$. To test the scaling of the time per computational step for a given dimension, we increase only that dimension successively by a factor of two until the problem is too large for available memory; the time per step is measured for each of these runs. The results are presented in Fig. 10. The N_x and N_y dimensions scale asymptotically as $N \log N$, as expected for fast Fourier transforms. The timestep is expected to scale with the number of grid points along the mean magnetic field as N_Z^2 because of the field solver. However, for practical problem sizes ($N_Z \lesssim 1000$), the field solver is still subdominant compared with the gyrokinetic solver. Therefore, we observe N_Z^c dependence with $c < 2$. In each of the dimensions N_{λ} , N_E , and N_s , the scaling is linear as anticipated. Thus, the wallclock time per step on a single processor scales as

$$t_{\text{step}} \propto (N_x \log N_x)(N_y \log N_y)(N_Z^c)(N_{\lambda})(N_E)(N_s). \quad (80)$$

5.2. Parallel performance scaling

Parallel performance of **AstroGK** is measured by taking the weak and strong scalings: The weak scaling is probed by holding the computational work per processing core constant while the number of cores, thus the total problem size, is increased. On the other hand, the strong scaling is probed by holding the problem size constant while the number of processing cores is increased. Both tests are performed on **Kraken** Cray XT5 system at the National Institute for Computational Sciences at the University of Tennessee. **Kraken** consists of 8256 compute nodes each having 12 processing cores, resulting in 99,072 compute cores in total.

The number of grid points is chosen such that parallelization is achieved efficiently in the layout ‘**yx1es**’. In fully developed kinetic turbulence, fine structure develops in velocity space as well as in position space, thus, it is required to take the same order of grid points in both spaces. The referenced maximum number of total grids is $256^2 \times 128^2$ for the current highest resolution runs [28]. Here, however, position-space resolution is taken relatively small in the strong scaling because of the memory requirement for small number of processors.

5.2.1. Weak scaling

The initial problem uses $(N_x, N_y, N_Z, N_{\lambda}, N_E, N_s) = (160, 160, 36, 6, 4, 2)$ on 12 processing cores. Each time the processing core count is doubled, the problem size is doubled by alternately doubling first N_E and then N_{λ} —since both of these dimensions scale linearly with the problem size, doubling one of these dimensions effectively doubles the computational work, leading to fair assessment of the weak scaling. The weak scaling behavior of the wallclock time per step t_{step} vs. the number of processing cores up to $N_{\text{proc}} = 12,288$ is plotted in Fig. 11. **AstroGK** follows the ideal scaling until $N_{\text{proc}} = 12,288$ with slight degradation of performance ($\sim 5\%$) due to the increase of communication for $N_{\text{proc}} > 1000$. The layout specified for the parallel communication for this test is ‘**yx1es**’.

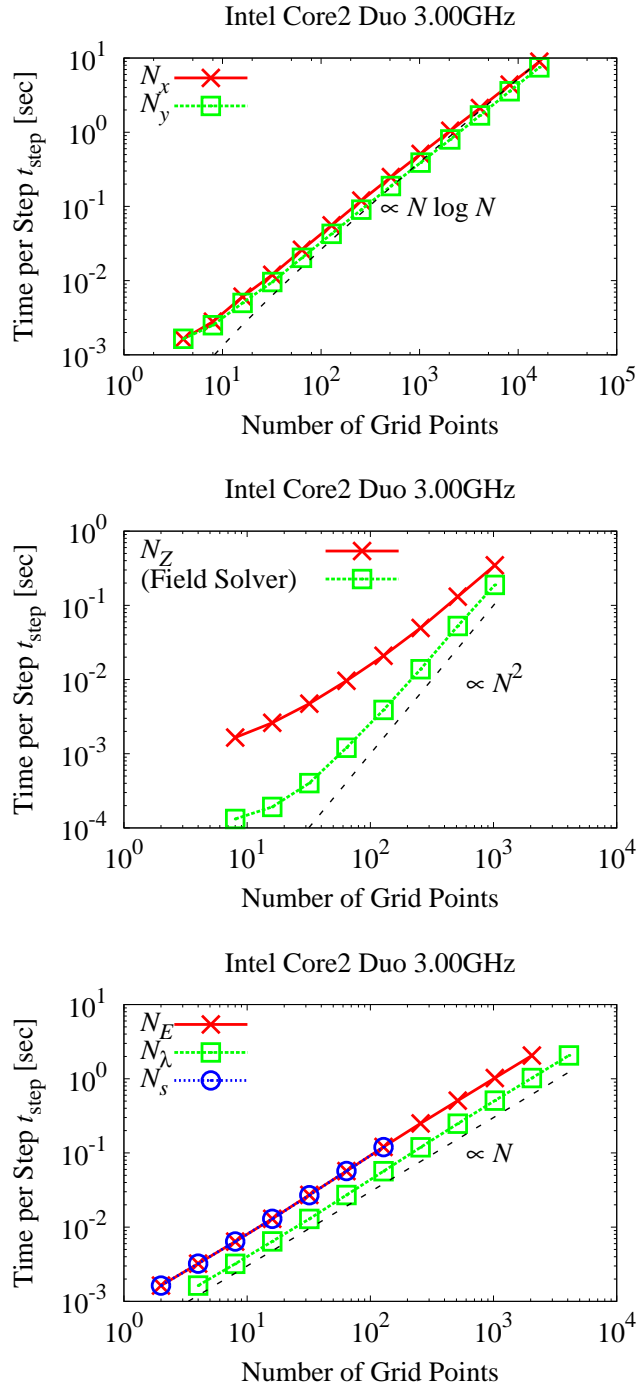


Figure 10: Single processor scaling of the time per step t_{step} vs. N , where N corresponds to; either the number of grid points N_x (crosses) or N_y (squares) in the top panel, N_Z in the middle panel, and either N_λ (crosses) or N_E (squares) or N_s (circles) in the bottom panel. The asymptotic scalings are achieved for $N_{x,y}$ as $N \log N$ (top), and for $N_{E,\lambda,s}$ as N (bottom). For N_Z scaling (middle), the asymptotic scaling is not achieved. The field solver scales as N_Z^2 , but is still subdominant for the practical problem size.

Weak Scaling @ Kraken [Cray XT5]

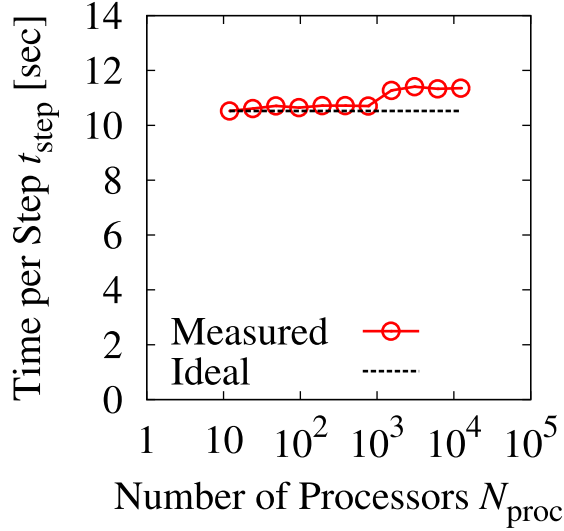


Figure 11: Weak scaling of `AstroGK` determined by holding the computational work per processor constant while the number of processors is increased. The time per step t_{step} vs. the number of processing cores N_{proc} is plotted.

5.2.2. Strong scaling

The dimensions of the nonlinear turbulence problem employed for this scaling are $(N_x, N_y, N_z, N_\lambda, N_E, N_s) = (32, 32, 24, 192, 256, 2)$. The strong scaling behavior of the wallclock time per step t_{step} vs. the number of processors N_{proc} is plotted from $N_{\text{proc}} = 48$ to $N_{\text{proc}} = 98,304$ in Fig. 12. Again, the layout specified for the parallel communication is ‘`yx1es`’.

To accommodate this large computational problem on a small number of processors requires more memory per core than is available when all 12 cores on a compute node are used. Therefore, for the lowest four data points on the scaling curve (up to 384 processors), only 1, 2, 4, and 8 core(s) are utilized per node. The rest of the runs all utilize 12 cores per node. As the number of cores per node increases, the computation time deviates from the ideal linear scaling (“Ideal (48)” line in the figure). The sharing of communication and memory bandwidth between multiple cores lead to a factor of two degradation of performance. If the number of cores per node is fixed at 12, we observe a nearly ideal strong scaling from $N_{\text{proc}} = 384$ up to $N_{\text{proc}} = 24,576$, as indicated by “Ideal (384)” line in the figure. Significant performance loss occurs only at $N_{\text{proc}} = 49,152$.

Strong Scaling @ Kraken [Cray XT5]

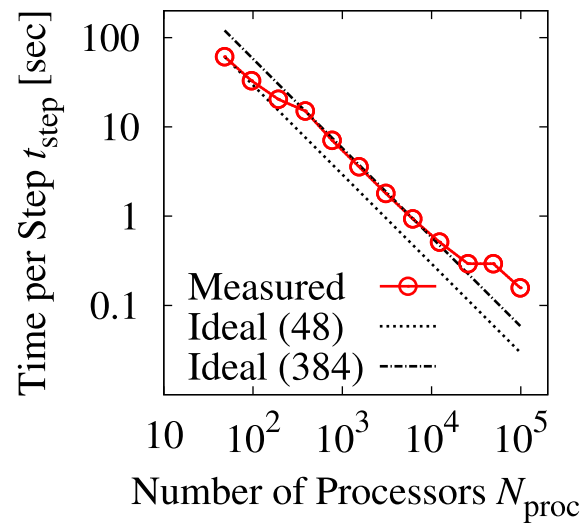


Figure 12: Plot of strong scaling taken by increasing the number of processors for the fixed problem size. The time per step t_{step} vs. the number of processors N_{proc} is shown. Ideal linear scaling lines compared with $N_{\text{proc}} = 48$ and $N_{\text{proc}} = 384$ are depicted.

6. Summary

We have presented detailed descriptions of the gyrokinetic-Maxwell equations solved in **AstroGK** and the algorithms adopted in the code. It employs an unconditionally stable implicit method for the linear terms and a third-order explicit multistep method for the nonlinear term. To reduce the computational cost for the implicit solve of the linear term, it utilizes the Godunov splitting method. Together with the Green's function approach developed by Kotschenreuther et al., **AstroGK** solves an $N_Z \times N_Z$ size linear system at each velocity grid point for each species. For collisionless runs, the overall accuracy of the algorithm is second order in Δt and second order in ΔZ , with spectral convergence for the velocity-space integration; for collisional runs, the velocity-space derivatives lead to a drop in the overall accuracy to first order in Δt and first order in the velocity-space integration.

The computational cost on a single processor follows the theoretical scaling except for the N_Z dependence. The time per computational step is expected to follow N_Z^2 because of the field solver for large N_Z . However, for practical problem sizes $N_Z \lesssim 1000$, the cost of the gyrokinetic solver is still larger or comparable with that of the field solver, and we do not observe the asymptotic scaling. Excellent parallel performance has also been demonstrated for both weak and strong scaling tests, showing the ideal scaling up to about 10,000 processors.

The algorithms at the heart of **AstroGK** are the same as those in **GS2**, but the **AstroGK** code has been streamlined by the removal of the magnetic geometry and trapped particle effects. Therefore, it is optimized for the study of fundamental, low-frequency kinetic effects in simple plasma geometries and for the exploration of the dynamics in many astrophysical plasmas of interest, in which the mean magnetic field at Larmor radius scales can often be well approximated as straight and uniform.

AstroGK is also an ideal developmental testbed, both for novel computational approaches and application to new physical plasma systems. One idea currently under development is the treatment of electrons as a fluid, since certain situations are indifferent to the kinetic behavior of the electrons. For instance, if one focuses on ion kinetic effects at scales $k_\perp \rho_i \sim 1$, the large ion-to-electron mass ratio $m_i/m_e \gg 1$ may lead to negligible electron kinetic effects in some cases. In [3], the isothermal electron fluid equations are given. Implementation of this alternative treatment of the electron dynamics in **AstroGK** will lead to dramatic improvements in computational speed for the study of ion kinetic effects.

One important aspect of **AstroGK** is its portability. It is designed to work on a wide range of computing environments, from individual desktop PCs to petascale supercomputers, and new users can easily port it to their particular computing environment. It also supports major FORTRAN 95 compilers. The potential drawback of this emphasis on portability is that it is not necessarily optimized to any particular architectures. Further efforts to optimize the code will be made to enhance both serial and parallel efficiency of the code.

Acknowledgments

This work is supported in part by the DOE Center for Multiscale Plasma Dynamics (Fusion Science Center Cooperative Agreement ER54785), the DOE Maryland Fusion Theory Research Program (DOE Grant No. DEFG0293-ER54197), the Leverhulme Trust Network for Magnetised Turbulence in Astrophysical and Fusion Plasmas, the Aspen Center for Physics, the Wolfgang Pauli Institute in Vienna, the National Science Foundation through TeraGrid resources provided by National Institute for Computational Sciences under Grant No. TG-PHY090084 and by the Texas Advanced Computing Center under Grant Nos. TG-AST030031N and TG-PHY090080.

Table A.1: Symbols in the gyrokinetic-Maxwell equations and their explanations, definitions and normalizations. The subscript s signifies the symbol is dependent on species, and Boltzmann's constant is absorbed to give temperature in units of energy.

Symbol	Explanation	Normalization
\mathbf{B}_0	Mean magnetic field	
$\hat{\mathbf{b}}_0 = \mathbf{B}_0/B_0$	Unit vector in mean field direction	
f_{0s}	Background Maxwellian dist. func.	
h_s	Non-Maxwellian part of dist. func.	$\varepsilon \hat{h}_s f_{0s}$
ϕ	Electrostatic potential	$\varepsilon \hat{\phi} (T_{00}/q_0)$
A_{\parallel}	Parallel component of vector potential	$\varepsilon \hat{A}_{\parallel} (v_{\text{th}0} T_{00}/q_0)$
δB_{\parallel}	Parallel component of magnetic field	$\varepsilon \delta \hat{B}_{\parallel} B_0$
m_s	Mass	$\hat{m}_s m_0$
q_s	Electric charge	$\hat{q}_s q_0$
n_{0s}	Density of the background	$\hat{n}_{0s} n_{00}$
T_{0s}	Temperature of the background	$\hat{T}_{0s} T_{00}$
ν_s	Collision Frequency	$\hat{\nu}_s (v_{\text{th},0}/a_0)$
$L_{B_0}, L_{n_{0s}}, L_{T_{0s}}$	Scales of the background	$\hat{L}_{B_0, n_{0s}, T_{0s}} a_0$
κ	Curvature of the mean field	$\hat{\kappa}/a_0$
$v_{\text{th},s} \equiv \sqrt{2T_{0s}/m_s}$	Thermal velocity	$\sqrt{\hat{T}_{0s}/\hat{m}_s} v_{\text{th}0}$
$v_{\text{th}0} \equiv \sqrt{2T_{00}/m_0}$	Reference thermal velocity	
$\Omega_s \equiv q_s B_0/m_s$	Cyclotron frequency	$(\hat{q}_s /\hat{m}_s) \Omega_0$
$\Omega_0 \equiv q_0 B_0/m_0$	Reference cyclotron frequency	
$\rho_s \equiv v_{\text{th},s}/\Omega_s$	Thermal Larmor radius	$(\sqrt{\hat{m}_s \hat{T}_{0s}}/ \hat{q}_s) \rho_0$
$\rho_0 \equiv \sqrt{2m_0 T_{00}}/(q_0 B_0)$	Reference thermal Larmor radius	
$d_s \equiv \sqrt{m_s}/(\mu_0 n_{0s} q_s^2)$	Inertial skin depth	$\sqrt{\hat{m}_s}/(\beta_0 \hat{n}_{0s} \hat{q}_s^2) \rho_0$
$\beta_s \equiv 2\mu_0 n_{0s} T_{0s}/B_0^2$	Plasma beta	$\hat{n}_{0s} \hat{T}_{0s} \beta_0$
$\beta_0 \equiv 2\mu_0 n_{00} T_{00}/B_0^2$	Reference plasma beta	
$\alpha_s = k_{\perp} V_{\perp}/\Omega_s$	Argument of the Bessel functions	
$b_s = (k_{\perp} \rho_s)^2/2$	Argument of Γ_n	
μ_0	Vacuum permeability	

Appendix A. Symbols, definitions, coordinate, and normalization

In this Appendix, we present complementary explanations of the symbols, coordinate systems, and normalizations used in Section 2. Table A.1 lists the symbols and their explanations, definitions, and normalizations.

Appendix A.1. Coordinate

In gyrokinetics, it is convenient to describe dynamics of the distribution function in the gyro-center coordinate $(\mathbf{R}_s, \mathbf{V}_s)$ rather than the particle coordinate (\mathbf{r}, \mathbf{v}) . The following equations:

$$\mathbf{R}_s = \mathbf{r} + \frac{\mathbf{v} \times \hat{\mathbf{z}}}{\Omega_s}, \quad \mathbf{V}_s = \mathbf{v}, \quad (\text{A.1})$$

define linear transformation of the particle coordinate to the gyro-center coordinate, called the *Catto transform* [9]. We consider the Cartesian coordinate in \mathbf{r} and \mathbf{R}_s :

$$\mathbf{r} = x\hat{\mathbf{x}} + y\hat{\mathbf{y}} + z\hat{\mathbf{z}}, \quad \mathbf{R}_s = X_s\hat{\mathbf{X}}_s + Y_s\hat{\mathbf{Y}}_s + Z_s\hat{\mathbf{Z}}_s, \quad (\text{A.2})$$

where $\hat{\mathbf{x}}, \hat{\mathbf{y}}$ and $\hat{\mathbf{X}}_s, \hat{\mathbf{Y}}_s$ are unit vectors that span the plane perpendicular to the mean field in $\hat{\mathbf{z}} = \hat{\mathbf{Z}}_s$.

Derivatives with respect to the position coordinate are equivalent ($\partial/\partial\mathbf{r} = \partial/\partial\mathbf{R}_s$), while those with respect to the velocity coordinate are different, which appears in the collision operators (See Appendix B and Refs. [32, 33]).

The velocity coordinate is written in two different ways in the text. In the gyrokinetic equation, we mainly use the polar coordinates ($V_{\parallel}, V_{\perp}, \Theta$): the relations to the Cartesian components are given by

$$V_{\perp} = \sqrt{V_x^2 + V_y^2}, \quad V_{\parallel} = V_z, \quad \tan \Theta = \frac{V_y}{V_x}, \quad (\text{A.3})$$

and $|\mathbf{V}| = V = \sqrt{V_{\perp}^2 + V_{\parallel}^2}$. It is convenient to write in energy and pitch-angle coordinates when the collision operator and velocity space integrals are considered:

$$E = V_{\perp}^2 + V_{\parallel}^2, \quad \lambda = \frac{V_{\perp}^2}{V^2 B_0}. \quad (\text{A.4})$$

Appendix A.2. Normalization

The GK-M equations solved by **AstroGK** are cast into dimensionless form through the normalization of all quantities with respect to the parameters of a reference species (denoted by the subscript 0), the mean magnetic field strength B_0 , and the parallel length scale a_0 .

The presence of a mean magnetic field leads to different characteristic temporal and spatial scales in the parallel and perpendicular directions. The length scale in the perpendicular plane is characterized by the thermal Larmor radius of the reference species, ρ_0 . The ratio of the perpendicular and parallel scales defines the small expansion parameter $\varepsilon \equiv \rho_0/a_0 \ll 1$ in gyrokinetic theory [1, 3]. Denoting normalized quantities with the “hat” symbol, we define the normalized length scales in perpendicular and parallel directions by $\hat{k}_{\perp} = k_{\perp}\rho_0$ and $\hat{k}_{\parallel} = k_{\parallel}a_0$. The time scale is normalized by the thermal crossing time of the reference species in the parallel direction, $\hat{t} = t/(a_0/v_{\text{th}0})$.

Species dependent quantities retain their species subscript s after normalization to the reference species, for example mass $\hat{m}_s = m_s/m_0$. The two-dimensional velocity space of distribution function g_s employs a species dependent normalization so that integrations over velocity space remain efficient even when characteristic thermal velocities of the plasma species differ by a large factor. The coordinates used in velocity space by **AstroGK** are the energy $E_s = (1/2)m_s v_s^2$ and pitch angle $\lambda_s = v_{\perp,s}^2/(v_s^2 B_0)$, which are related to the magnetic moment by $\lambda_s E_s = m_s v_{\perp,s}^2/(2B_0)$. Normalizing the velocity to the species thermal velocity $\hat{\mathbf{v}}_s = \mathbf{v}/v_{\text{th},s}$, the dimensionless velocity space coordinates are given by $\hat{E}_s = \hat{v}_s^2$ and $\hat{\lambda}_s = \hat{v}_{\perp,s}^2/\hat{v}_s^2$.

The first-order fluctuating quantities in the GK-M equations are the distribution function for each species g_s and the electromagnetic field variables: the scalar potential ϕ , the parallel component of the vector potential A_{\parallel} , and the parallel component of the magnetic field δB_{\parallel} . The distribution function is normalized by

$$\hat{g}_s = \frac{g_s a_0}{f_{0s} \rho_0}, \quad (\text{A.5})$$

where $f_{0s}/f_{00} = \hat{n}_{0s} \exp(-\hat{v}_s^2) / (\pi^{3/2} \hat{v}_{\text{th},s}^3)$ with $f_{00} = n_{00}/v_{\text{th}0}^3$. The fields are normalized by

$$\hat{\phi} = \frac{a_0 q_0 \phi}{\rho_0 T_{00}}, \quad \hat{A}_{\parallel} = \frac{a_0}{\rho_0} v_{\text{th}0} \frac{q_0 A_{\parallel}}{T_{00}}, \quad \delta \hat{B}_{\parallel} = \frac{a_0}{\rho_0} \frac{\delta B_{\parallel}}{B_0}. \quad (\text{A.6})$$

Notice that the dimensionless normalizations for all fluctuating, first-order quantities are also multiplied by a factor a_0/ρ_0 so that all normalized terms have unity order of magnitude.

An illustration of the normalization of velocity space integrals in Maxwell’s equations follows for the integral $\int g_s d\mathbf{v}$. To normalize the integral, we multiply by $1/(v_{\text{th}0}^3 f_{00})(a_0/\rho_0)$ to obtain $\hat{n}_{0s} \int (e^{-\hat{v}_s^2}/\pi^{3/2}) \hat{g}_s d\hat{\mathbf{v}}_s$.

Appendix B. Model collision operator

In this Appendix, we present the model collision operator employed in **AstroGK**. This complements the overview of the numerical implementation given in Section 3.3.4.

AstroGK uses the model Fokker–Planck collision operator given in [32, 33], which includes the effects of pitch-angle scattering and energy diffusion while satisfying Boltzmann’s H -Theorem and conserving particle number, momentum, and energy. Upon gyro-averaging, the same-species collision operator is written in the spectral representation as

$$\mathcal{C}_{k_\perp}(h_{\mathbf{k}_\perp}) = \mathcal{C}_L(h_{\mathbf{k}_\perp}) + \mathcal{C}_D(h_{\mathbf{k}_\perp}) + \mathcal{U}_L(h_{\mathbf{k}_\perp}) + \mathcal{U}_D(h_{\mathbf{k}_\perp}), \quad (\text{B.1})$$

where

$$\mathcal{C}_L(h_{\mathbf{k}_\perp}) = \frac{\nu_D(v/v_{\text{th}})}{2} \left(\frac{\partial}{\partial \xi} (1 - \xi^2) \frac{\partial h_{\mathbf{k}_\perp}}{\partial \xi} - \frac{k_\perp^2 v^2}{2\Omega^2} (1 + \xi^2) h_{\mathbf{k}_\perp} \right), \quad (\text{B.2})$$

and

$$\mathcal{C}_D(h_{\mathbf{k}_\perp}) = \frac{1}{2v^2} \frac{\partial}{\partial v} \left(\nu_{\parallel}(v/v_{\text{th}}) v^4 f_0 \frac{\partial h_{\mathbf{k}_\perp}}{\partial v} \frac{1}{f_0} \right) - \nu_{\parallel}(v/v_{\text{th}}) \frac{k_\perp^2 v^2}{4\Omega^2} (1 - \xi^2) h_{\mathbf{k}_\perp}, \quad (\text{B.3})$$

are the gyro-averaged Lorentz and energy diffusion operators, respectively. Together, these form the exact test-particle piece of the linearized Landau operator. The velocity-dependent collision frequencies ν_D and ν_{\parallel} are given by

$$\nu_D(x) = \nu \frac{\Phi(x) - G(x)}{x^3}, \quad \nu_{\parallel}(x) = \frac{2\nu G(x)}{x^3}, \quad (\text{B.4})$$

with $\Phi(x) = (2/\sqrt{\pi}) \int_0^x \exp(-y^2) dy$ the error function, $G(x) = (\Phi(x) - x d\Phi/dx)/(2x^2)$ the Chandrasekhar function, and $\nu = \sqrt{2}\pi n_0 q^4 \ln \Lambda / (m^{1/2} T_0^{3/2})$ the same-species collision frequency, which is an input parameter.

The test-particle operator given above does not conserve particle momentum and energy, so the additional terms \mathcal{U}_L and \mathcal{U}_D are added to recover conservation properties. Care is taken in choosing the form of these conservation terms so that Boltzmann’s H -Theorem is respected. With these constraints, one obtains:

$$\mathcal{U}_L(h_{\mathbf{k}_\perp}) = \nu_D f_0 \left(J_0(\alpha) v_{\parallel} \frac{\int \nu_D v_{\parallel} J_0(\alpha) h_{\mathbf{k}_\perp} d\mathbf{v}}{\int \nu_D v_{\parallel}^2 f_0 d\mathbf{v}} + J_1(\alpha) v_{\perp} \frac{\int \nu_D v_{\perp} J_1(\alpha) h_{\mathbf{k}_\perp} d\mathbf{v}}{\int \nu_D v_{\parallel}^2 f_0 d\mathbf{v}} \right), \quad (\text{B.5})$$

and

$$\begin{aligned} \mathcal{U}_D(h_{\mathbf{k}_\perp}) = & -\Delta\nu f_0 \left(J_0(\alpha) v_{\parallel} \frac{\int \Delta\nu v_{\parallel} J_0(\alpha) h_{\mathbf{k}_\perp} d\mathbf{v}}{\int \Delta\nu v_{\parallel}^2 f_0 d\mathbf{v}} + J_1(\alpha) v_{\perp} \frac{\int \Delta\nu v_{\perp} J_1(\alpha) h_{\mathbf{k}_\perp} d\mathbf{v}}{\int \Delta\nu v_{\parallel}^2 f_0 d\mathbf{v}} \right) \\ & + \nu_E v^2 J_0(\alpha) f_0 \frac{\int \nu_E v^2 J_0(\alpha) h_{\mathbf{k}_\perp} d\mathbf{v}}{\int \nu_E v^4 f_0 d\mathbf{v}}, \end{aligned} \quad (\text{B.6})$$

where the additional collision frequencies $\Delta\nu$ and ν_E are defined as

$$\Delta\nu = \nu_D - 2(v/v_{\text{th}})^2 \nu_{\parallel}, \quad (\text{B.7})$$

$$\nu_E = -(\nu_{\parallel} + 2\Delta\nu). \quad (\text{B.8})$$

The terms \mathcal{U}_L and \mathcal{U}_D are treated separately in **AstroGK** so that the Lorentz and energy diffusion operators can be split with the conservation properties and H -Theorem maintained within each splitting. When combined, these conserving terms constitute an approximation to the field-particle piece of the linearized Landau operator.

The effect of ion–electron collisions are neglected in `AstroGK` because they are small in the electron–ion mass ratio. However, electron–ion collisions are comparable in size to same-species collisions, so they are retained. Consequently, the electron collision operator has the following additional term:

$$\mathcal{C}^{\text{ei}}(h_{\mathbf{k}_{\perp},\text{e}}) = \mathcal{C}_{\text{L}}^{\text{ei}}(h_{\mathbf{k}_{\perp},\text{e}}) + \nu_{\text{D}}^{\text{ei}} \frac{2v_{\parallel} u_{\parallel,\text{i}}}{v_{\text{th,e}}^2} J_0(\alpha_{\text{e}}) f_{0\text{e}}, \quad (\text{B.9})$$

where $u_{\parallel,\text{i}}$ is the perturbed ion parallel flow velocity, and $\mathcal{C}_{\text{L}}^{\text{ei}}$ and $\nu_{\text{D}}^{\text{ei}}$ are obtained from their same-species counterparts by replacing the same-species collision frequency ν with the inter-species collision frequency.

Appendix C. Laplace–Fourier solution for driven gyrokinetics

We derive a Laplace–Fourier solution for time dependence of the A_{\parallel} amplitude for a driven gyrokinetic system in this Appendix. The solution presented here is for linear, collisionless gyrokinetics without δB_{\parallel} , the nonlinear term, and the linear driving terms, and with an external driving force given by

$$A_{\parallel}^{\text{antenna}} = \begin{cases} A_{\parallel 0} e^{-i(\omega_0 t - \mathbf{k}_0 \cdot \mathbf{x})} & t \geq 0 \\ 0 & t < 0 \end{cases}. \quad (\text{C.1})$$

We also set $n_{0i}/n_{0e} = -q_i/q_e = 1$ for simplicity. Given the driving parameters used in the code, the solution should agree with a result obtained from the code without free parameters.

Performing a Laplace transform in time and a Fourier transform in space on this system of equations, we can solve for the Laplace–Fourier transformed distribution function for the driven Fourier mode (without the species index s):

$$\tilde{g}_{\mathbf{k}_{\perp 0}} = \frac{g_{\mathbf{k}_{\perp 0}}(0)}{p + ik_{\parallel 0} V_{\parallel}} - \frac{qf_0}{T_0} J_0(\alpha_0) \left[\frac{ik_{\parallel 0} V_{\parallel} \tilde{\phi}_{\mathbf{k}_{\perp 0}}}{p + ik_{\parallel 0} V_{\parallel}} + \frac{V_{\parallel} \left(p \tilde{A}_{\parallel, \mathbf{k}_{\perp 0}} - A_{\parallel, \mathbf{k}_{\perp 0}}(0) \right)}{p + ik_{\parallel 0} V_{\parallel}} \right] \quad (\text{C.2})$$

where $\alpha_0 = k_{\perp 0} V_{\perp} / \Omega$. Setting the initial conditions to zero, $g_{\mathbf{k}_{\perp 0}}(0) = A_{\parallel, \mathbf{k}_{\perp 0}}(0) = 0$, and substituting into Maxwell's equations, we obtain:

$$\begin{pmatrix} H & K \\ H - K & b_{i0}/\bar{\omega}^2 \end{pmatrix} \begin{pmatrix} \bar{E}_{\parallel} \\ \bar{A}_{\parallel} \end{pmatrix} = \begin{pmatrix} 0 \\ -(b_{i0}/\bar{\omega}^2) \bar{S} \end{pmatrix} \quad (\text{C.3})$$

where we have used the following definitions to simplify the notation:

$$\bar{E}_{\parallel} = \tilde{\phi}_{\mathbf{k}_{\perp 0}} - \frac{ip \tilde{A}_{\parallel, \mathbf{k}_{\perp 0}}}{k_{\parallel 0}}, \quad \bar{A}_{\parallel} = \frac{ip \tilde{A}_{\parallel, \mathbf{k}_{\perp 0}}}{k_{\parallel 0}}, \quad (\text{C.4})$$

$$H = \sum_s \frac{T_{0i}}{T_{0s}} (1 + \Gamma_{0s} \zeta_s \Xi(\zeta_s)), \quad K = \sum_s \frac{T_{0i}}{T_{0s}} (1 - \Gamma_{0s}), \quad (\text{C.5})$$

$$\bar{S} = \frac{ip A_{\parallel 0} / k_{\parallel 0}}{p + i\omega_0}, \quad \bar{\omega} = \frac{ip}{k_{\parallel 0} v_A}, \quad (\text{C.6})$$

$b_{i0} = (k_{\perp 0} \rho_i)^2 / 2$, $v_A = B_0 / \sqrt{\mu_0 n_{0i} m_i}$, $\zeta_s = ip / (k_{\parallel 0} v_{\text{th}, s})$, and Ξ is the plasma dispersion function [47]. The dispersion relation:

$$p^2 + [Q(p)]^2 = p^2 + \frac{b_{i0} H k_{\parallel 0}^2 v_A^2}{HK - K^2} = 0 \quad (\text{C.7})$$

leads to the Alfvén wave solutions.

Now we will focus on the solution for $A_{\parallel, \mathbf{k}_{\perp 0}}(t)$. The Laplace–Fourier solution is

$$\tilde{A}_{\parallel, \mathbf{k}_{\perp 0}}(p) = -\frac{[Q(p)]^2 A_{\parallel 0}}{(p^2 + [Q(p)]^2)(p + i\omega_0)}. \quad (\text{C.8})$$

To proceed further, we make the approximation:

$$p^2 + Q^2 \simeq (p + i\omega_1)(p + i\omega_2), \quad (\text{C.9})$$

where $\omega_{1,2}$ are the complex eigenfrequencies independent of p ; we know for this system these solutions typically have the form $\omega_1 = \omega_r + i\omega_i$, $\omega_2 = -\omega_r + i\omega_i$ with a negative growth rate $\omega_i < 0$. With this simplification, the inverse Laplace transform is easily found by application of the residue theorem to find:

$$\frac{A_{\parallel, \mathbf{k}_{\perp 0}}(t)}{A_{\parallel 0}} = \frac{[Q(-i\omega_0)]^2 e^{-i\omega_0 t}}{(\omega_1 - \omega_0)(\omega_2 - \omega_0)} + \frac{[Q(-i\omega_1)]^2 e^{-i\omega_1 t}}{(\omega_0 - \omega_1)(\omega_2 - \omega_1)} + \frac{[Q(-i\omega_2)]^2 e^{-i\omega_2 t}}{(\omega_0 - \omega_2)(\omega_1 - \omega_2)}. \quad (\text{C.10})$$

Note that the second and third term will decay with time. This solution is computed numerically for comparison to code results, as presented in Section 4.1.1.

References

- [1] G. G. Howes, S. C. Cowley, W. Dorland, G. W. Hammett, E. Quataert, A. A. Schekochihin, Astrophysical gyrokinetics: Basic equations and linear theory, *Astrophys. J.* 651 (1) (2006) 590–614.
- [2] G. G. Howes, S. C. Cowley, W. Dorland, G. W. Hammett, E. Quataert, A. A. Schekochihin, A model of turbulence in magnetized plasmas: Implications for the dissipation range in the solar wind, *J. Geophys. Res.* 113 (2008) A05103.
- [3] A. A. Schekochihin, S. C. Cowley, W. Dorland, G. W. Hammett, G. G. Howes, E. Quataert, T. Tatsuno, Astrophysical gyrokinetics: Kinetic and fluid turbulent cascades in magnetized weakly collisional plasmas, *Astrophys. J. Suppl. Series* 182 (1) (2009) 310–377.
- [4] <<https://sourceforge.net/projects/gyrokinetics/>>.
- [5] L. D. Landau, On the vibrations of the electronic plasma, *Zh. Eksp. Teor. Fiz.* 16 (7) (1946) 574–586 (in Russian; English translation in *J. Phys. USSR* 10 (1) (1946) 25–34).
- [6] A. Barnes, Collisionless damping of hydromagnetic waves, *Phys. Fluids* 9 (8) (1966) 1483–1495.
- [7] P. H. Rutherford, E. A. Frieman, Drift instabilities in general magnetic field configurations, *Phys. Fluids* 11 (3) (1968) 569–585.
- [8] J. B. Taylor, R. J. Hastie, Stability of general plasma equilibria – I formal theory, *Plasma Phys.* 10 (5) (1968) 479–494.
- [9] P. J. Catto, Linearized gyro-kinetics, *Plasma Phys. Control. Fusion* 20 (7) (1978) 719–722.
- [10] T. M. Antonsen, Jr., B. Lane, Kinetic equations for low frequency instabilities in inhomogeneous plasmas, *Phys. Fluids* 23 (6) (1980) 1205–1214.
- [11] P. J. Catto, W. M. Tang, D. E. Baldwin, Generalized gyrokinetics, *Plasma Phys.* 23 (7) (1981) 639–650.
- [12] E. A. Frieman, L. Chen, Nonlinear gyrokinetic equations for low-frequency electromagnetic waves in general plasma equilibria, *Phys. Fluids* 25 (3) (1982) 502–508.
- [13] D. H. E. Dubin, J. A. Krommes, C. Oberman, W. W. Lee, Nonlinear gyrokinetic equations, *Phys. Fluids* 26 (12) (1983) 3524–3535.
- [14] T. S. Hahm, W. W. Lee, A. Brizard, Nonlinear gyrokinetic theory for finite-beta plasmas, *Phys. Fluids* 31 (7) (1988) 1940–1948.
- [15] A. Brizard, Nonlinear gyrofluid description of turbulence magnetized plasmas, *Phys. Fluids B* 4 (5) (1992) 1213–1228.
- [16] H. Sugama, Gyrokinetic field theory, *Phys. Plasmas* 7 (2) (2000) 466–480.
- [17] A. J. Brizard, T. S. Hahm, Foundations of nonlinear gyrokinetic theory, *Rev. Mod. Phys.* 79 (2) (2007) 421–468.
- [18] M. Kotschenreuther, G. Rewoldt, W. M. Tang, Comparison of initial value and eigenvalue codes for kinetic toroidal plasma instabilities, *Comput. Phys. Commun.* 88 (2-3) (1995) 128–140.
- [19] Z. Lin, T. S. Hahm, W. W. Lee, W. M. Tang, R. B. White, Turbulent transport reduction by zonal flows: Massively parallel simulations, *Science* 281 (5384) (1998) 1835–1837.
- [20] W. Dorland, F. Jenko, M. Kotschenreuther, B. N. Rogers, Electron temperature gradient turbulence, *Phys. Rev. Lett.* 85 (26) (2000) 5579–5582.
- [21] F. Jenko, W. Dorland, M. Kotschenreuther, B. N. Rogers, Electron temperature gradient driven turbulence, *Phys. Plasmas* 7 (5) (2000) 1904–1910.
- [22] J. Candy, R. E. Waltz, An Eulerian gyrokinetic-Maxwell solver, *J. Comput. Phys.* 186 (2) (2003) 545–581.
- [23] S. E. Parker, Y. Chen, W. Wan, B. I. Cohen, W. M. Nevins, Electromagnetic gyrokinetic simulations, *Phys. Plasmas* 11 (5) (2004) 2594–2599.
- [24] T.-H. Watanabe, H. Sugama, Velocity-space structures of distribution function in toroidal ion temperature gradient turbulence, in: *Proceedings of the 20th IAEA Fusion Energy Conference*, No. TH/8-3Rb, Villamoura, Portugal, 1-6 November, 2004. (IAEA, Vienna, Austria, 2004).
- [25] V. Grandgirard, Y. Sarazin, P. Angelino, A. Bottino, N. Crouseilles, G. Darnet, G. Dif-Pradalier, X. Garbet, P. Ghendrih, S. Jolliet, G. Latu, E. Sonnendrücker, L. Villard, Global full- f gyrokinetic simulations of plasma turbulence, *Plasma Phys. Control. Fusion* 49 (12B) (2007) B173–B182.
- [26] Y. Idomura, M. Ida, T. Kano, N. Aiba, S. Tokuda, Conservative global gyrokinetic toroidal full- f five-dimensional Vlasov simulation, *Comput. Phys. Commun.* 179 (6) (2009) 391–403.
- [27] G. G. Howes, W. Dorland, S. C. Cowley, G. W. Hammett, E. Quataert, A. A. Schekochihin, T. Tatsuno, Kinetic simulations of magnetized turbulence in astrophysical plasmas, *Phys. Rev. Lett.* 100 (6) (2008) 065004.
- [28] T. Tatsuno, W. Dorland, A. A. Schekochihin, G. G. Plunk, M. Barnes, S. C. Cowley, G. G. Howes, Nonlinear phase mixing and phase-space cascade of entropy in gyrokinetic plasma turbulence, *Phys. Rev. Lett.* 103 (1) (2009) 015003.
- [29] T. Tatsuno, M. Barnes, S. C. Cowley, W. Dorland, G. G. Howes, R. Numata, G. G. Plunk, A. A. Schekochihin, Gyrokinetic simulation of entropy cascade in two-dimensional electrostatic turbulence, *J. Plasma Fusion Res. Ser.* 9 (2010) 509–516. <arXiv:1003.3933>.
- [30] R. Numata, W. Dorland, G. G. Howes, N. F. Loureiro, B. N. Rogers, A. A. Schekochihin, T. Tatsuno, Gyrokinetic simulations of tearing instability – from collisional to collisionless regimes, unpublished results.
- [31] K. D. Nielson, G. G. Howes, T. Tatsuno, R. Numata, W. Dorland, Numerical modeling of Large Plasma Device Alfvén wave experiments using AstroGK, *Phys. Plasmas* 17 (2) (2010) 022105.
- [32] M. Barnes, I. G. Abel, W. Dorland, D. R. Ernst, G. W. Hammett, P. Ricci, B. N. Rogers, A. A. Schekochihin, T. Tatsuno, Linearized model Fokker–Planck collision operators for gyrokinetic simulations II. numerical implementation and tests, *Phys. Plasmas* 16 (7) (2009) 072107.
- [33] I. G. Abel, M. Barnes, S. C. Cowley, W. Dorland, A. A. Schekochihin, Linearized model Fokker–Planck collision operators for gyrokinetic simulations I. theory, *Phys. Plasmas* 15 (12) (2008) 122509.

- [34] R. Courant, K. Friedrichs, H. Lewy, On the partial differential equations of mathematical physics, *Math. Ann.* 100 (1928) 32–74 (in German; English translation in *IBM J. Res. Devel.* 11 (2) (1967) 215–234).
- [35] M. Abramowitz, I. A. Stegun (Eds.), *Handbook of Mathematical Functions with Formulas, Graphs, and Mathematical Tables*, Dover Publications, New York, 1972 (Chapter 25.4. Integration, pp. 885–896).
- [36] M. Barnes, W. Dorland, T. Tatsuno, Resolving velocity space dynamics in continuum gyrokinetics, *Phys. Plasmas* 17 (3) (2010) 032106.
- [37] S. K. Godunov, A difference method for numerical calculation of discontinuous solutions of the equations of hydrodynamics, *Math. Sbornik* 47 (89) (1959) 271–306 (in Russian).
- [38] G. Strang, On the construction and comparison of difference schemes, *SIAM J. Numer. Anal.* 5 (3) (1968) 506–517.
- [39] R. M. Beam, R. F. Warming, Implicit finite-difference algorithm for hyperbolic systems in conservation-law form, *J. Comput. Phys.* 22 (1) (1976) 87–110.
- [40] E. A. Belli, Studies of numerical algorithms for gyrokinetics and the effects of shaping on plasma turbulence, Ph.D. thesis, Princeton University (2006).
- [41] J. Sherman, W. J. Morrison, Adjustment of an inverse matrix corresponding to changes in the elements of a given column or a given row of the original matrix, *Ann. Math. Stat.* 20 (4) (1949) 621.
- [42] J. Sherman, W. J. Morrison, Adjustment of an inverse matrix corresponding to a change in one element of a given matrix, *Ann. Math. Stat.* 21 (1) (1950) 124–127.
- [43] S. A. Orszag, On the elimination of aliasing in finite-difference schemes by filtering high-wavenumber components, *J. Atmos. Sci.* 28 (6) (1971) 1074.
- [44] T. H. Stix, *Waves in Plasmas*, Springer-Verlag, New York, 1992.
- [45] L. I. Rudakov, R. Z. Sagdeev, On the instability of a nonuniform rarefied plasma in a strong magnetic field, *Dokl. Akad. Nauk SSSR* 138 (3) (1961) 581–583 (in Russian; English translation in *Sov. Phys. -Dokl.* 6 (5) (1961) 415–417).
- [46] T. Antonsen, B. Coppi, R. Englade, Inward particle transport by plasma collective modes, *Nucl. Fusion* 19 (5) (1979) 641–658.
- [47] B. D. Fried, S. D. Conte, *The Plasma Dispersion Function*, Academic Press, New York, 1961.
- [48] S. I. Braginskii, *Transport Processes in a Plasma*, *Reviews of Plasma Physics*, vol. 1, Consultants Bureau, New York, 1965, pp. 205–311.
- [49] H. P. Furth, J. Killeen, M. N. Rosenbluth, Finite-resistivity instabilities of a sheet pinch, *Phys. Fluids* 6 (4) (1963) 459–484.
- [50] L. Spitzer, *Physics of Fully Ionized Gases*, Interscience, New York, 1956.
- [51] R. Fitzpatrick, F. Porcelli, Collisionless magnetic reconnection with arbitrary guide field, *Phys. Plasmas* 11 (10) (2004) 4713–4718.
- [52] S. A. Orszag, C.-M. Tang, Small-scale structure of two-dimensional magnetohydrodynamic turbulence, *J. Fluid Mech.* 90 (1) (1979) 129–143.